Order Number 9119665

Synchronization issues regarding the meteor burst communication channel

Parsa, Kourosh, Ph.D.

City University of New York, 1991

U·M·I
300 N. Zeeb Rd.
Ann Arbor, MI 48106

A

SYNCHRONIZATION ISSUES REGARDING THE METEOR BURST COMMUNICATION CHANNEL

BY: KOUROSH PARSA

A dissertation submitted to the Graduate Faculty in Engineering in partial fulfillment of the requirement for the degree of Doctor of Philosophy

The City University of New York

1991

This manuscript has been read and accepted for the Graduate Faculty in Engineering in satisfaction of the dissertation requirement for the degree of Doctor of Philosophy

10/18/90
Date

Chair of Examining Committee

10/19/90
Date

Executive Officer

J. Barba

P. Karmel

T. Saadawi

N. Scheinberg

D. R. Vaman

Supervisory Committee

The City University of New York

ACKNOWLEDGEMENT

I wish to express sincere gratitude to my mentor Professor Donald L. Schilling for his guidance and help during the course of this research.

Many thanks to my loving wife Shideh for her continuous support and patience.

I wish to express my appreciation to my family for believing in me and encouraging me in every step of my entire education.

Table of Contents

LIST OF ILLUSTRATIONS

1 INTRODUCTION

1.1 CONTRIBUTIONS AND EXECUTIVE SUMMARY

Interest in high-throughput, high-speed digital communications using the meteor scatter channel has necessitated detailed studies of the channel multipath structure and the phase perturbations, primarily because a coherent modem's performance is dependent on timing and phase jitter. The coherent demodulation process entails two key functions: 1) clock recovery by the bit synchronizer, and 2) phase and frequency acquisition and tracking by the carrier recovery circuit. Timing jitter is a measure of the accuracy of the recovered clock, whereas phase jitter corresponds to a phase offset (error) in estimating the phase of the recovered carrier. Multipath spread is the source of timing uncertainty, which in turn effects the timing jitter suffered by the bit synchronizer in the coherent receiver.

This dissertation is concerned with resolving the following problem: How does an adaptive coherent modem perform over the meteor burst (MB) channel? More specifically, to what extent do the MB channel conditions such as time spread and phase perturbation degrade the coherent modem's performance? To alleviate this problem, the following issues must be addressed.

1) Identification of MB phase perturbations;

2) Design of an adaptive coherent modem;

3) Computation of the phase and timing jitter at the coherent receiver;

4) Derivation of a jitter loss(timing and phase) formula;

5) Incorporation of jitter losses into the MB communication system's throughput; and

6) Derivation of maximum-bits-per-burst bound for the proposed modems.

We begin with a brief historical overview of meteor scatter research and systems, and preview the main theme of this work in **chapter one**. In **chapter two**, we establish a unified, commu-

nication engineering point of view on glint theory, specular reflection condition, doppler spread, and multipath spread, providing a solid framework for the subsequent research. Doppler spread had been considered in conjunction with wind velocity measurement in the upper atmosphere, and only for back-scatter links in the fifties. **The first contribution of our work is characterization of the MB doppler spread for the forward scatter links [Eq. 2.2.3]. In this context, it is shown that doppler spread is a function of trail position, wind velocity and the link distance.**

In **chapter 3**, we identify and characterize all sources of MB perturbations. In investigating the effects of wind on the trail distortion mechanism, we have found a doppler rate created by the continuous shift of the specular reflection point on the trail. Here, doppler rate is a function of trail position, trail orientation , the link distance, and the wind gradient [Eq. 3.1.2]. **The discovery of the doppler rate induced phase perturbation mechanism and its characterization constitute the second contribution of this work.** As for the head-echo phenomenon, formerly researched solely in context of meteor velocity measurements, we have used Manning's "moving ball" model to characterize a head-echo induced phase perturbation. This perturbation is a sinusoidal jitter, with its frequency being a function of meteor velocity, trail position, orientation, and the link distance. **Equations 3.2.7 and 3.2.11 represent another important contribution which is the characterization of the head-echo phase changes for the forward scatter links.**

Having characterized the MB doppler spread and MB phase perturbations, in **chapter 4** we present a **new MB channel model** through the introduction of a **new formula** [Eq. 4.2.4]. This formula is an analytical expression of the MB phase perturbations.

In the first part of this study (chapters 2-4), a new MB channel model is developed. This is achieved by characterizing the MB doppler spread, doppler rate, head-echo induced

phase jitter, and deriving new and simple mathematical expressions for them. The new MB channel model lays the foundation for developing high data-rate adaptive systems , and permit waveform coding and design for the band-limited meteor burst channel to be systematically approached and resolved, as well as can function as a basis of comparison for the performance of various modulation-coding schemes.

Carrier and clock recovery are two functions performed by PLL in any coherent receiver. **Chapter 5** surveys the PLL's acquisition and tracking mode performance, including such parameters as thermal noise phase jitter in the tracking mode, the frequency and phase acquisition time, and the timing jitter in the bit synchronizer. Having characterized the MB phase and timing jitter, we determine the optimum (minimizing the phase error) value for B_l in section 5.6.

Chapter six is devoted to deriving a **new formula** [Eq. 6.0.8] to establish the relationship between phase and timing offset (ϕ_0, τ_0), and the SNR penalty (jitter loss=Δ). This formula applies to the M-ary PSK modulation scheme.

In **chapter seven**, we present a sample system, a typical wind velocity vector, wind gradient, meteor velocity, trail position and orientation. We also present the operation principles for adaptive and fixed rate meteor burst modems. We compare the performance of the two modems employed in such a system and under the specified channel conditions. It is shown that a fixed-rate modem (QPSK rate 7/8) outperforms the adaptive coherent modem.

Furthermore, a **new throughput formula [Eq. A.7] is derived in appendix A in which the average data rate is expressed in terms of modulation-dependent parameters.**

In the second part of this study (chapters 5-7), the new MB channel model is used to investigate the feasibility of building high-speed adaptive coherent modems. To do so, we compute the phase and timing jitter at a typical adaptive coherent receiver. A jitter loss formula [Eq.6.0.8] is then derived which expresses the SNR penalty as a function of timing

and phase offsets for MPSK. The jitter loss is then incorporated into the MB communication system's throughput performance, and finally a maximum-bits-per-burst bound is derived for a sample system. It is shown that MB channel impairments can cause an effective 46% reduction in the average data rate (throughput) for the given adaptive coherent modem and the sample system.

1.2 BACKGROUND AND FUNDAMENTALS

Meteor burst communication exploits the ionization trails left behind by billions of particles which enter the earth's atmosphere daily. Experimental evidence suggests that the number of incoming meteors is inversely proportional to their mass. The usable meteors, which weigh in the range of 10^{-1} to 10^{-4} g and have average diameters of .2 to 2 mm, are divided into two categories: shower and sporadic meteors.

Shower meteors occur in groups and appear only at certain times of the year, when their orbits intercept that of the earth. These showers are numerous during these short periods, during which time they can significantly enhance communication. However, shower meteors account for a small fraction of the total annual incident meteor flux.

Sporadic meteors are far more numerous and move in random orbits around the sun. This results in a continuous 'drizzle' of meteors which in turn causes a high background level of ionization trails. These trails enable meteor scatter to be a viable communications method throughout the year. Although statistical information on the geographic distribution of trails is incomplete, there is sufficient knowledge to allow their gross attributes to be predicted, and to determine their likely system performance.

Although radiants -- those areas of the sky from which the meteors appear to originate-- and the actual timing of each event are random, the overall arrival rate shows a seasonal variation of 4:1 between the maximum in August and minimum in February. A 4:1 variation is also observed at temperate latitudes, following a diurnal, roughly sinusoidal cycle, with the greatest number of trails being observed at 0600 and the least at 1800 local time, all due to the earth's rotation [23]. This feature arises because on the morning side the earth 'sweeps up' more meteors, while in the evening only those meteors which overtake the earth give rise to trails. The flux of

incoming meteors and the degree of diurnal variation both decrease with increasing latitude. However, all these generalized trends reflect long-term averaged behavior, and there is extensive short-term variation in the incidence of both sporadic and shower meteors.

As the meteors enter the atmosphere, frictional heating and collisional excitation result in the formation of long, thin ionization trails. This process kicks off when the meteors encounter relatively dense air at around 120 km altitude. The majority of these meteors evaporate by 85 km. Although the trails can measure up to 40 km in length, the average length is 15 km. The initial radii of the trail lie in the range of .5 to 4.0 m. After their formation, the trails expand by diffusion and are distorted by wind so that they dissipate in a short time (from few milliseconds to a few seconds). Individual trails thus possess relatively short useful lifetimes. This is one central feature of meteor burst (MB) communications. Since the medium is intermittent, transmission must proceed by concatenating data transferred over successive trails.

It is the electron density of the trail which determines its efficacy for communications. Density is a function of both the mass and the velocity (12-72 km/sec) of the incoming meteors. Electron line densities of $10^{10} - 10^{16}$ electrons/m will give a useful scattering of radio waves. Within this range, the trails are traditionally classified as underdense or overdense, with the dividing boundary set at 10^{14} electrons/m. Up to 10^{14} e/m (underdense trails) radio waves pass through the ionized region with relatively little modification and the scattering is evaluated by summing the individual scattered components. For overdense trails, the physical scattering process needs a different description because inter-electron coupling cannot be ignored; the radio waves, after initial, slight penetration of the trail, are completely reflected. Signals propagated via overdense trails have different characteristics than their underdense analogues. They have both higher amplitudes and longer usable lifetimes. However, the underdense trails are far more numerous.

Scattering at the meteor trails is specular. Successful transmission can be achieved when the trail axis is tangential to any ellipsoid which has the transmitter and receiver as foci, as shown diagrammatically in Fig. 1.1.1. The tangency condition, combined with the distribution of the trail radiants at altitudes of 80-100 km, results in certain parts of the sky being favoured over others. Regions of increased meteor activity are called 'hot spots'.

The signal scattered by any particular underdense trail is only received in a restricted area- the footprint- which may be typically up to 20x50 km in extent. The inherent privacy of MB communication is due to the relatively small ground illumination footprint of individual meteor trails. The region on the ground illuminated by a trail is a function of the length of the trail and its location and orientation relative to the geometry of the link [24]. Figure 1.1.2 illustrates how the footprint changes as the trail location varies.

Frequencies in the range of 30-100 MHz can be supported by meteor scatter. To date most systems have employed values between 35 and 50 MHz. The choice of the operating frequency is determined by three major factors. At low frequencies both the received power and the total number of trails giving echos increases. Non-derivative absorption within the D and lower F regions of the ionosphere follows an inverse square law dependence and is therefore greatest for lower frequencies. The third factor supporting the use of higher frequencies is the need to avoid interference from ionospherically scattered and refracted signals which may increase the noise level by the introduction of co-channel interference.

MB Systems can be deployed in many diverse applications. These include remote surveillance, meteorological and environmental data from both ground stations and buoys, emergency and rapid deployment communications, primary and back-up communication in the geographically distributed auroral and polar cap regions, and military communications. The latter includes

ground-to-ground, ground-to-air and ground-to-sea communications in both point-to-point and networked systems.

Figure 1.1.1 :The link geometry [5]

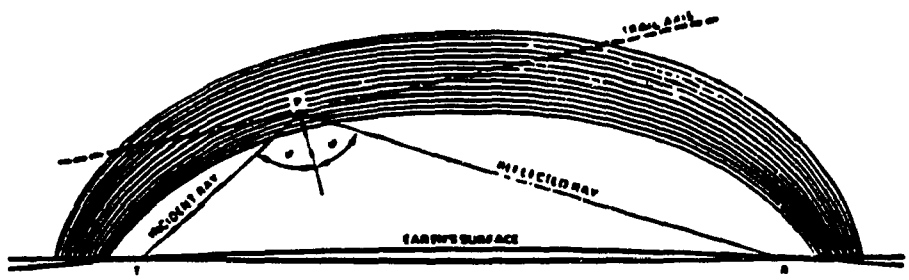

Figure 1.1.2:Effect of trail location on size of ground illumination footprint.[24]

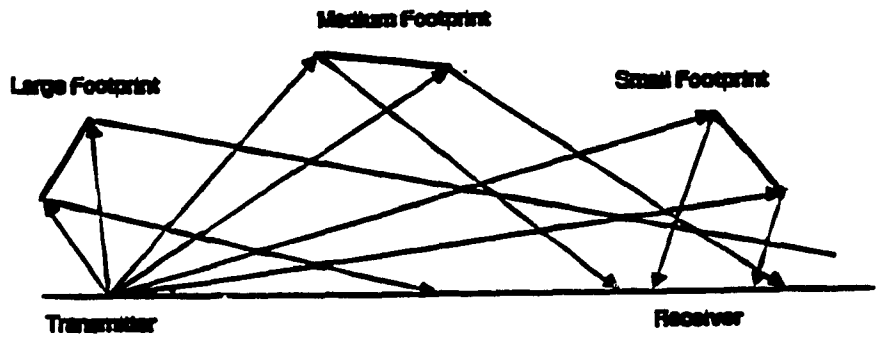

1.3 PREVIOUS SYSTEMS

The very first MB system was the Canadian system JANET-B (named after JANUS the Roman god who looked both ways) which was deployed in 1954. JANET was a full duplex system operating on two frequencies close to 40 MHz and separated from each other by approximately 1 MHz. The radiant power was 500 W, which fed an array of four 5-element Yagis. The system used binary amplitude modulation. The link protocol was set up in the following manner. Initially, both stations radiated unmodulated carriers on separate frequencies, and at each station the receiver continuously monitored the remote station frequency. When a meteor trail formed in a suitable location to scatter the signal, each receiver could potentially hear the appropriate remote carrier and, if this exceeded a predetermined level, a 650 Hz tone was transmitted. Only then was data transmitted in either direction. The transmission loop was broken either when the SNR fell below 12 dB, the detection threshold, or when the output storage facility was filled. The instantaneous data rate was 650 bits/sec and the average daily data rate was 15 bits/sec in July/August.

Hannum et Al [26] were the first to design an air-to-ground simplex MB Communication System which used ARQ. The transmitter power was 5000 W and the modulation scheme was FSK. The instantaneous data rate was 2000 bits/sec and the average daily data rate was 15 bits/sec. This system was built in 1959.

COMET(COmmunications by MEteor Trails) was built at SHAPE Technical Center in the Hague in 1966. It was over a 1000 km path between the Netherlands and southern France [25]. The system utilized an FSK modulation technique and incorporated ARQ. It operated with 200 W transmitter power and a 2000 bits/sec data rate. The daily average data rate was 115 bit/sec in December.

During the late 1970's and early 1980's two systems, SNOTEL and AMBCS were deployed for operational use. SNOTEL (SNOpac TELemetry) has been operational since 1978 and is used by the United State Department of Agriculture to collect, when polled, snow precipitation and temperature data from remote unattended solar-powered terminals. This data is then used for water resource planning. SNOTEL remains the prime example of a large MB network covering ten adjacent western states, using 600 remote stations and 2 master stations. AMBCS (Alaska Meteor Burst Communications System) is used by five U.S. Federal agencies with diverse applications including retrieval of weather data, maintenance of contact with survey camps, collection of water, snow and river data, and collection of wind and wave data from the Gulf of Alaska. All of these services are provided from a single master station in Anchorage which covers the entire state of Alaska.

Most recently a new system has been developed in England. The system is known as BLOSSOM-A(Beyond Line of Sight Signalling Over Meteors), and is designed for air-to-ground radio communications. Ground-to-ground trials of this system started during early 1986 over an 800km link from the town of Wick to Farnborough. This system uses ARQ, FSK modulation, a 4-element Yagi antenna, 650 W transmitter power and a 37 MHz carrier frequency. This simplex system operates at 2000 bits/sec and its average daily data rate is 20 bits/sec.

Above, we have illustrated the salient features of existing MB systems. Of these, the COMET system performance stands out, especially considering the power level used. The designers of the system related the enhanced performance to the space and frequency diversity.

The Hannum system used more than ten times the power of other systems, and yet it did not match the performance of the low power systems. We can identify two causes for the conspicuous low throughput of these systems: the first is, the low duty cycle which can be

attributed to an inefficient antenna pattern design, and the second, is the constant bit-rate systems which must be replaced with adaptive bit-rate systems. This dissertation is ultimately concerned with the implementation of adaptive systems.

1.4 HISTORICAL OVERVIEW

Several eminent scientists including, Lindeman and Dobson [27], C.M. Sparrow, H.B. Maris, and J. Hoppe, contributed to the development of the classical physical theory of meteors during the period 1920-1940. Perhaps the greater share of the credit should go to two men: **E.J. Opik** [28],who displayed a great insight into the details of the physical processes, and **F.L. Whipple** [29], who supplied accurate observational material and further streamlined the theory. The historical highlights are covered in several summary papers, notably by Whipple [29], and Herlofson [3]. The classical theory of meteors combines conventional aerodynamic ballistics with plausible assumptions about atomic collisions and light emission processes. It was from this theory that Whipple derived amazingly accurate estimates of the air densities and temperatures at meteoric heights from his photographic observations of meteor luminosities and decelerations. Furthermore, the developments in meteor ionization theory have stemmed directly from the classical theory. **The following is a synopsis of the salient features of the meteor theory.**

The shape, mass, and density of the meteoroid are all unknown. **As the meteor travels through the atmosphere, it's front surface is subject to bombardment by air molecules, a great portion of which are trapped in the metal surface, giving up their kinetic energy.** The kinetic energy of the meteoroid is converted into heat, light, and ionization, though the fraction which appears as heat greatly exceeds the other two. Atoms of the meteoroid are vaporized from the surface of the parent body. The heat supplied by this process is sufficient to bring the meteor to the temperature of evaporation and the meteor atoms then distill off the meteor with thermal velocities relative to the meteor surface. **The light and ionization are produced by subsequent collisions when the evaporated meteor atoms are slowed down**

by air molecules.

Various processes for the ablation of atoms may be envisioned, which are conditioned by the composition and size of the meteoroid and the height at which the action is taking place. When the mean free path of the air particles is greater than the radius of the meteoroid, the atoms leave the body without serious mutual interference. Lower down in the atmosphere, a shielding effect may arise, owing to a layer of vaporized atoms about the meteoroid. Lower still in the atmosphere, and particularly for larger bodies, an air cap may develop ahead of the meteoroid. These considerations are fully developed by Opik [28]. Whatever the mechanism, it is assumed that **the rate of loss of mass is proportional to the kinetic energy transferred to the intercepted air mass.** The ablated atoms move with the velocity of the meteoroid, and hence their kinetic energies range from a few tens to some hundreds of electron volts. This kinetic energy is more than adequate to excite and also to ionize the atoms of the meteor, for which typical excitation or ionization potentials range from about 2 to 15 ev. The excited atoms emit light and the ionized atoms scatter the incident radio waves.

The MB communication channel was discovered in 1931 by G.W. Pickard [1]. However, it was not until 1946 that a clear correlation between radio signals and individual meteor trails was reported [2]. By the late 40's, communication engineers became interested in the meteor propagation phenomenon. This period saw the peak of meteor scatter research. During the 50's research proceeded in two general directions: The propagation characteristics of the meteor trails [5], and the use of meteors as a tool for ionospheric research [6].

In a classic paper, Sugar surveyed those characteristics of meteors and meteor propagation which pertain to meteor ionization as it provides a means of radio transmission [5]. Ionospheric research provided detailed measurements of atmospheric density and temperature, diffusion coefficient, wind velocity, and turbulence at altitudes of 80-100 km. The state of knowledge in

meteor communication and meteor theory was surveyed in a book by McKinnley in the middle 60's [4]. The technology at that time provided limited storage and signal-processing capability, so that meteor communication systems were of limited usefulness. Moreover, satellites became the technology of choice for long-range communication. By the late 1960's, interest in meteor communication had waned. During the 1970's meteor scatter research was primarily scientific, using meteor trail echos to characterize the middle atmosphere.

Findings during this period represent current knowledge: As a meteor burns up, it produces a trail of positive ions and free electrons, forming tubular clouds. Once the meteoric matter reaches thermal equilibrium with air molecules, the ionization trail will expand by **ambi-polar diffusion; electrons follow the heavier positive ions because of electric attraction.**

Meteors as small as 10^{-5} grams will produce a trail which is visible by radio, as long as the line defining the axis of the tubular meteor trail is tangential to an ellipsoid of revolution with foci at the receiver and the transmitter [4]. This point defines the center of the region of constructive interference known as the first, or principal, Fresnel zone. In addition to the geometric constraint, for the trail to be radio observable there must be significant ionization at the point of tangency.

The most frequently observed meteoric propagation mechanism is the underdense meteor trail. These trails are formed by micrometeors with masses from about 10^{-5} to 10^{-3} grams. **Underdense trails have sufficiently low electron density such that an incident wave can pass through the trail.** Each electron in the trail scatters the incident electromagnetic wave independently of all other electrons in the trail. The echoing area or the scattering cross section of a free electron is $\sigma_e = 4\pi r_e^2 \sin^2\gamma$, where r_e is the classical electron radius and γ is the angle between the electric vector of the incident wave and the line of sight to the receiver. The scattered wave from any given electron is in phase with the incident wave. The total reflected wave is

therefore the vector sum of many coherent and monochromatic wavelets. The radial expansion of the trail causes destructive interference and exponential decay of the received power.

As the electron density increases, the trail appears less like a tubular cloud and more like a plasma cloud. These are overdense trails. **The model for propagation is more complicated than that for underdense trails due to the complicated interaction between electrons. Exact closed form solution for the return from overdense trails is not yet formulated.** Hines and Forsythe [43] assumed that the trails are so dense that there is perfect reflection from the surface of an expanding tubular metallic cylinder. The received power due to the reflection from an overdense trail approximated by Hines and Forsythe is often used and sited in the meteor scatter literature. Figure 1.3.1 contains samples of underdense, overdense and nonspecular overdense signals.

In recent years the perceived vulnerability of satellite-based communication systems, coupled with improvements in technology, and especially inexpensive microprocessor-based systems, has led to a resurgence of interest in both HF and meteor scatter. Meteor channels were also found to provide a relatively new, uncongested, and extremely directional means of communications. Meteor scatter utilizes higher frequencies than HF (40-100 MHz for meteor scatter versus 2-30 MHz for HF), so it is less subject to absorption and blackout conditions which frequently occur at high latitudes. The meteor propagation mechanism does not depend on ionospheric reflection, so a single frequency can be used for the operation of the network.

In contrast HF requires both a number of frequency allocations and frequency management to adapt to temporal variations in the maximum usable frequency of the ionosphere. Finally, because the scattering area of a meteor trail is smaller than that of the HF layer , the ground illumination footprint of the meteor trail is smaller than that of HF; therefore, meteor channels provide inherent protection against ground-based intercepters and jammers.

The need for high throughput meteor scatter systems necessitates incorporating recent technological innovations, which in turn have prompted new research efforts. This dissertation is one product of such efforts. The anticipated end result is state of the art communication system using meteor channels. To see how far we have come requires a survey of meteor scatter research over the past decade.

Figure 1.3.1: underdense, overdense, unspecular overdense signals [56]

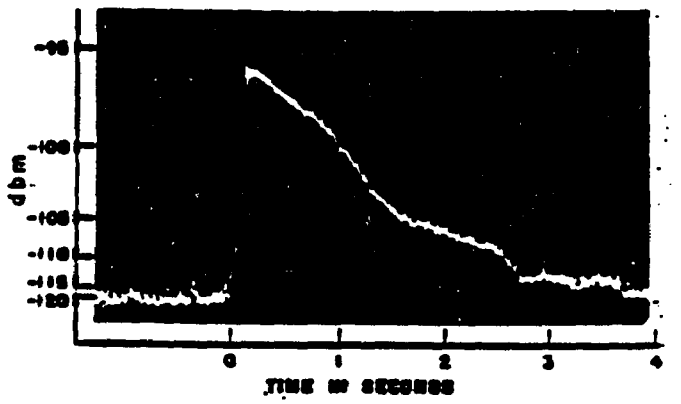

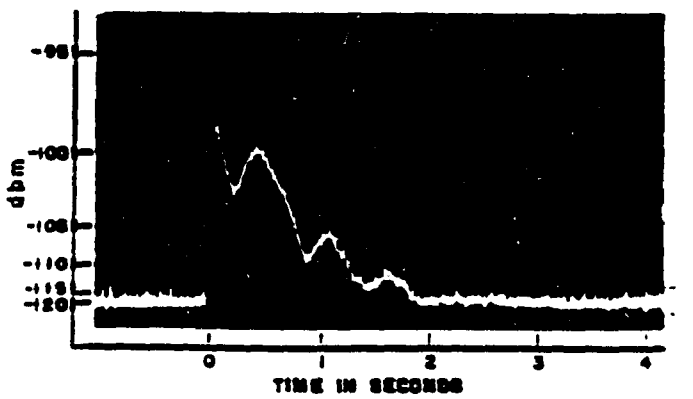

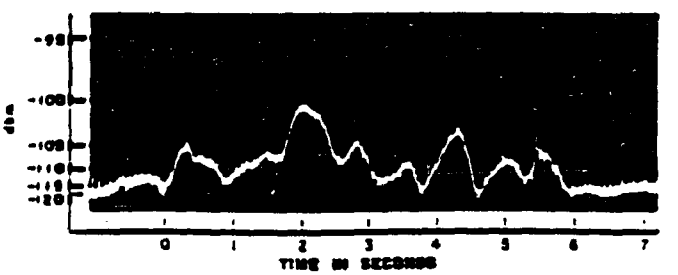

1.5 PREVIOUS RESEARCH

A survey of the recent meteor scatter research indicates that work is proceeding in two directions: gaining more insight into the propagation characteristics and mechanisms of the channel and developing technology and techniques for MB communications.

The propagation research includes exploring the complicated interaction between meteor spatial arrival pattern and the receiver-transmitter antenna patterns [30-31]; investigating the effect of the Faraday rotation [32]; characterizing the multipath, doppler spreads and fading profiles of auroral scatter and sporadic-E in addition to meteor trails [7],[34]; and observing the effect of polar cap absorption on meteor scatter link [33]. **Communication research** include estimate of the capacity of the meteor scatter channel [35], antenna and protocol design [36], coded versus uncoded transmissions [37], digital signal design for the channel [38], Feedback Adaptive Variable Rate (FAVR) technology for high data rate modems [39], adaptive information rate systems [40], variable code-rate modems [41], variable symbol rate modems [42].

Weitzen [31] presented a new meteor arrival model which includes improvements such as the capability to calculate antenna patterns to any desired degree of complexity, the inclusion of terms which compensate for the increase in activity due to meteor showers and seasonal increases, and the ability to consider polarization coupling and Faraday rotation loss. The new model was successfully employed to investigate the range dependence of the MB channel and the effect of various antenna patterns on system performance [36]. This model used a non-uniform spatial arrival distribution of meteor trails derived from the basic distribution of meteor orbits. Weitzen [36] asserted that at short ranges (300 km separation), large regions above and to the rear of the stations contribute heavily to the duty cycle.

At high latitudes, propagation phenomena such as sporadic-E and auroral scatter can alter

the communication characteristics of the MB channel. Weitzen et Al [34] characterized the doppler spread, multipath spread, and fading profile of the high latitude MB channel. When present, sporadic-E reflections exhibit low multipath spread, slow fading, and high signal levels. Due to its low predictability, this channel is considered the 'bonus' channel. Typical doppler spreads are less than 10 Hz. The primary source of multipath on the sporadic channel is the occurrence of meteor trails which produces intermittent spreads up to 1 ms. In an experiment on a 640km link from Anchorage to Bethel in Alaska, rms multipath spreads as high as 1 ms with doppler spreads in excess of 200 Hz were observed when auroral scatter was the primary propagation mechanism [34]. Both mechanisms transform the MB channel into a multipath-limited channel.

There are two multipath mechanisms identified on a MB channel. Manning [6] showed that high-altitude wind shears could warp the trail so that secondary areas satisfy the geometric condition for geometric scatter. This mechanism can result in a delay spread as high as several microseconds for long trails [44]. Simultaneous occurrence of more than one trail on a link can cause multipath in excess of 1-2 ms, depending on the geometry [45]. This phenomenon is only observed on less than one to two percent of the trails [45]. The bandwidth limitation due to this channel multipath structure is therefore on the order of a few hundred kHz. However, in the United States, the frequencies useful for meteor burst communications are often allocated in 20 kHz wide channels [46]. Therefore, the MB system bandwidth limitation is regulatory.

Milstein et al [47] used the probability of completing a given message as the performance measure of two protocols. In the first protocol, the transmitter is presumed to have knowledge (obtained by an appropriate probe signal) of the entire duration of a given MB. In the second, only the starting time of each MB is known. The channel arrival process was modelled as a Poisson density with an average arrival time between bursts a function of required SNR, and

with exponentially distributed burst durations independent of SNR. To evaluate the probability of completing the message, several Reed Solomon (RS) codes, each with a different code rate, were considered. It was shown that the first protocol requires much less waiting time. Furthermore, the researchers found that the packet size should equal the average duration of a burst in order to maximize the throughput. The efficacy of forward error correction coding was also analyzed [47]. They considered RS codes with rates of 1/3, 1/2, and 2/3. They concluded that at high SNRs, a high-rate code is desirable, whereas at low SNRs , the error-correction capability of the low-rate code becomes the dominant consideration. Furthermore, for constant bit-rate systems, it was shown that error correction codes do not significantly improve the system performance. For example, an uncoded system operating at an SNR of 13 dB performs at about the same level as the (31,15,8) RS coded system operating at 8dB. Djuknic [37] further explored the coding aspects of this work and showed that hybrid FEC-ARQ strategy yields higher throughputs, lower waiting times, and an increased probability of correct packet reception as compared to uncoded transmission when the code rate approached 1. He employed convolutional codes in his analysis.

Exponential decay of the received signal to noise ratio is the primary reason that adaptive rate systems are more efficient than constant rate systems. A theoretical optimum MB communication system (regulatory bandwidth-limited) can be defined as follows: it is a system that changes the duration of each bit transmitted during a trail such that the energy of each bit remains constant. The information rate is primarily chosen on the basis of the received signal strength.

Schilling, et al [48] presented the Feedback Adaptive Variable Rate (FAVR) system in which a feedback channel is maintained to allow the transmitted bit rate to mimic the time behavior of the received power. FAVR is the practical embodiment of the optimum system. A crucial assumption in FAVR operation is the fact that reciprocity exists in the channel, i.e., the signal

power seen at the transmitter and receiver are the same. It was shown that by changing the bit rate as the power level was decreased by 3 dB, the throughput of the FAVR system approached 70% of the optimum system. A more complicated algorithm presented by the authors yields 83% efficiency.

Abel [40] used the received power equations for underdense and overdense trails to derive two deterministic maximum-bits-per-burst estimates for each meteor trail type. The bound used by Abel is the maximum number of bits that can be relayed by each burst under various operating conditions. Two bounds were derived using 1) an optimum constant bit rate, and 2) a continuously varying bit rate. Abel established that using a continuously varying bit rate rather than an optimum constant bit rate increases the maximum bits per burst by a factor of 2 to 3.

Pursley, et al [41] investigated the performance of variable-rate RS coding for MB communications. The code rate was varied from codeword to codeword within each packet. Optimum rates for the codewords are determined as a function of the length of the message and the decay rate for the meteor trail. They showed that the throughput can be improved by a factor of 1.42 on trails with a decay constant $\tau = .1$, by using optimal variable rate coding.

Jacobsmeyer [41] proposed an adaptive information rate scheme that uses trellis-coded modulation (TCM) and three M-ary PSK signal sets. He demonstrated that throughput improvement of more than a factor of 3 is possible. The improvement factor is defined as the ratio of the adaptive TCM over the fixed rate throughput. Indeed, if no drawbacks are associated with employing TC-8PSK and TC-16PSK, this work can bridge the gap between the theory and practise of adaptive meteor burst systems.

2 THEORETICAL FRAMEWORK

This chapter presents (from a communications engineering perspective) a view of glint theory, doppler spread, specular scatter condition, and multipath spread.

2.1 GLINT THEORY

The fading effects observed in overdense trails are due to interference between the waves scattered from two or more echoing points on the trail. The mechanism proposed to account for these discrete scattering centers is covered by the glint theory [6]. The glint theory assumes that the ionization is produced continuously and smoothly along the trail. Wind shears and turbulence in the upper atmosphere distort the trail more and more as time goes on (figure 2.1.1). The trail is warped, forming a complex serpentine shape. Whenever the tangent to a curved section of the trail becomes normal to the radar line of sight, a new scattering point (glint) is created. This is the so called tangency condition for the radar case at three time instants (figure 2.1.1).

The air motion that causes trail distortion was studied by both radar and photographic methods. The radar results were based primarily on doppler-shifted echoes from short-duration, non-fading echoes [9]. It was shown that the major wind components were horizontal and that the winds were stratified in height. Whipple [50] was able to photograph the contortions of long-enduring meteor trails. From the existing photographic and radar results, it appears reasonable that the vertical profile of a horizontal wind component in the ionosphere can be described as a sample of a gaussian function. Figure 2.1.2 is a histogram of the wind velocity at meteoric heights [51]. It is also assumed that the wind profile does not change for the duration of an echo.

Figure 2.1.1: The glint theory showing how additional reflecting points appear on the trail as a distortion progresses.

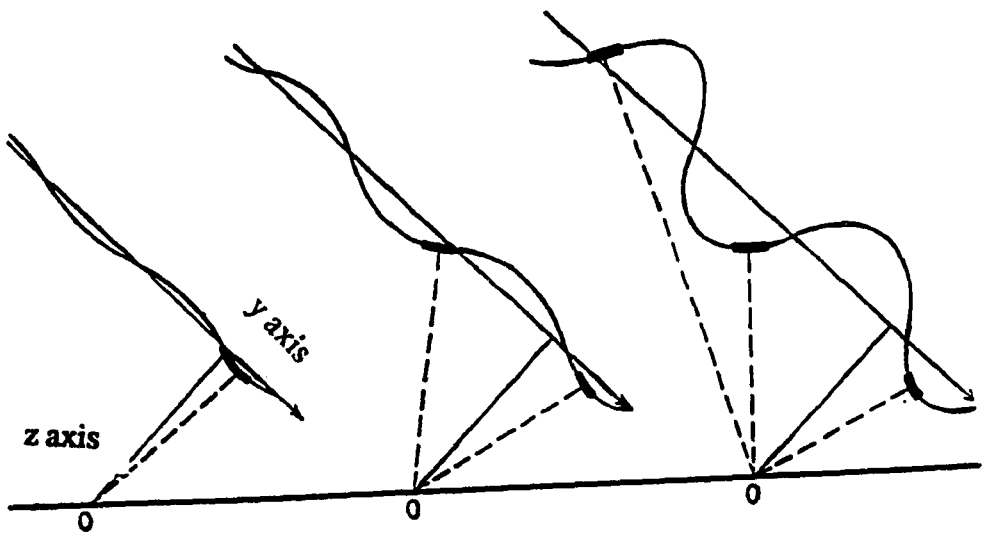

Figure 2.1.2: Histogram of the wind velocity at meteoric heights [51].

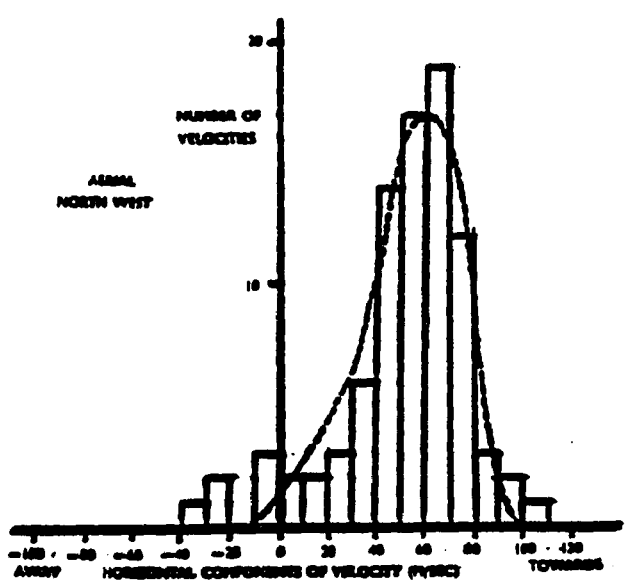

2.2 DOPPLER SPREAD

To characterize the doppler spread for the forward scatter meteor links, we consider a Cartesian coordinate system shown in Fig. 2.2.1 with the origin at the midpoint of the transmitter-receiver base line. The direction from the origin to the receiver represent the positive X axis. The Z axis represents the direction from the origin to the center of the earth, and the Y axis is defined by the requirements for a right-hand coordinate system. We assume a transmitter located at (-d,0,0) and a primary receiver located at (d,0,0) relative to this coordinate system. (x_t, y_t, z_t) is the point of tangency. Let

$$\vec{R}_T = -[(x_t + d)\hat{a}_x + y_t\hat{a}_y + z_t\hat{a}_z] \tag{2.2.1}$$

and

$$\vec{R}_R = -[(x_t - d)\hat{a}_x + y_t\hat{a}_y + z_t\hat{a}_z] \tag{2.2.2}$$

represent vectors from the tangent point to the transmitter at (-d,0,0) and the receiver at (d,0,0), respectively.

The zone on the trail where the signal is scattered, is subjected to wind shear, which causes the scatterer to move at wind velocity [6]. The moving scatterer causes a doppler shift of

$$f_W = \frac{\left(v_{\vec{R}_T} + v_{\vec{R}_R}\right)}{\lambda} \tag{2.2.3}$$

where $v_{\vec{R}_T}$ and $v_{\vec{R}_R}$ are wind velocities towards the transmitter and receiver respectively, and λ is the wavelength of the incident wave. The wind velocity vector is given by

$$\vec{v} = \hat{a}_x v_x + \hat{a}_y v_y \tag{2.2.4}$$

Equations (1),(2),(4) are combined to yield

$$v_{\vec{R}_T} = \frac{(\vec{R}_T \cdot \vec{v})}{R_T} = \frac{((x_t + d)v_x + v_y y_t)}{R_T} \tag{2.2.5}$$

and

$$v_{\vec{R}_R} = \frac{(\vec{R}_R \cdot \vec{v})}{R_R} = \frac{((x_t - d)v_x + v_y y_t)}{R_R} \tag{2.2.6}$$

Using Eq. 2.2.3, Figures 2.2.2 and 2.2.3 were developed to illustrate how the doppler spread changes as a function of the scattering point's location and the link distance. The results are for the wind velocity vector $\vec{v} = 100\hat{a}_x + 100\hat{a}_y$ m/sec. An important observation is that f_W peaks and then levels off in regions above and to the rear of the stations. This implies that MB links designed to capture the meteor trails above and to the rear of the stations are subjected to a higher constant doppler offset. The doppler shift imposes a lower limit on the loop bandwidth of the carrier recovery circuit in a coherent receiver.

Figure 2.2.1: Cartesian coordinate system

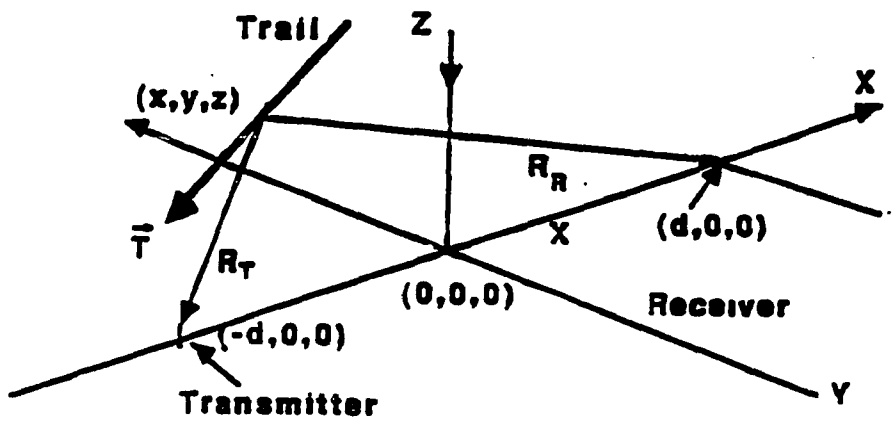

Figure 2.2.2: Doppler Spread vs.link distance and trail location for $v_x = 100m/\sec$ and $(x_t, y_t, z_t) = (x_t, 0, 100km$

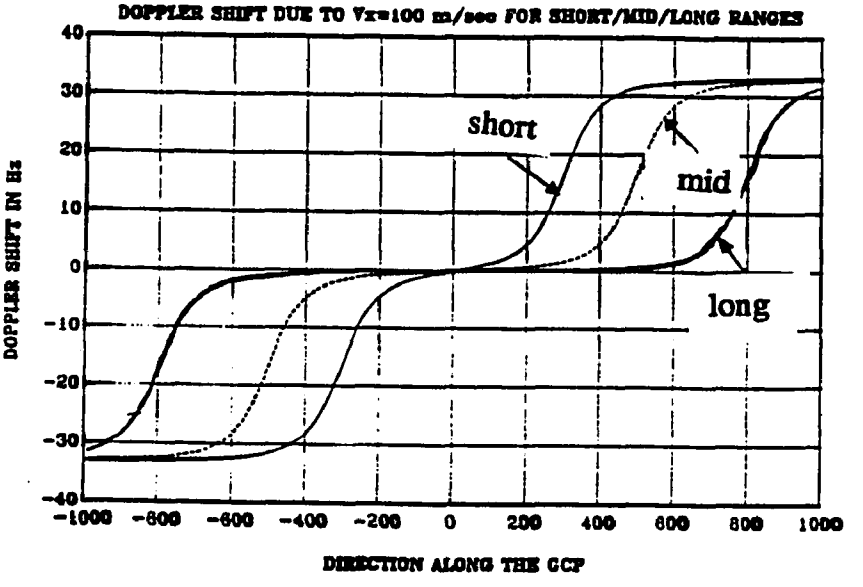

Figure 2.2.3: Doppler spread vs. link distance and trail location for $v_y = 100m/\sec$ and location.

$(x_t, y_t, z_t) = (x_t, 40km, 100km)$

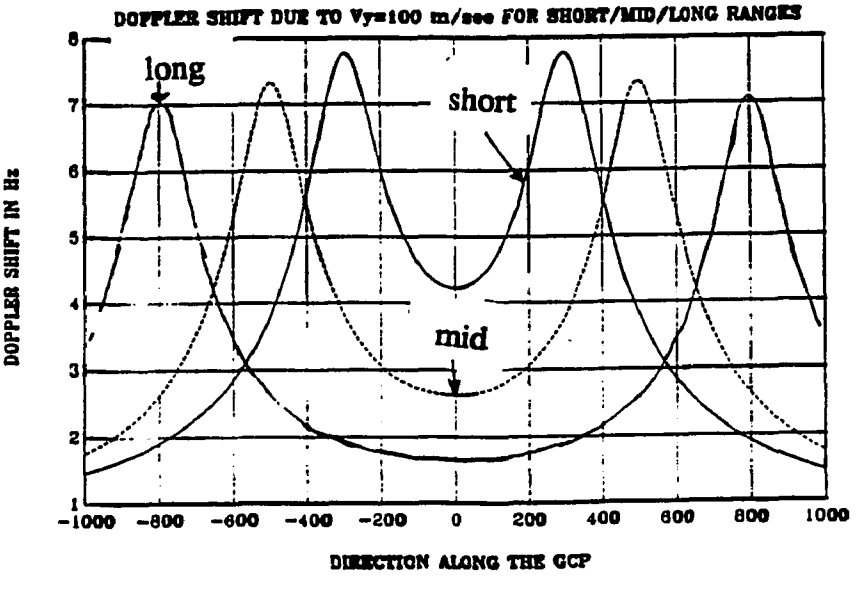

2.3 SPECULAR SCATTER CONDITION

According to the specular scatter trail model [6], differences in direction and magnitude of wind velocity as a function of height cause the initially straight trail to assume a serpentine form. The shape of the trail reproduces that of the wind profile. As time advances, the trail distortion increases, but the shape continues to be that of the wind profile. For specular scatter [see Fig. 2.1.2] from the distorted meteor trail, the tangent line to the curved section ($\vec{T}$) of the trail must be tangential to an ellipsoid with foci at receiver and transmitter. It is a property of the prolate spheroid that the bisector of the angle 2ϕ between R_T and R_R is normal to $\vec{T}$ [4]. Rudie [52] showed that the normal to an ellipsoid with foci at receiver and transmitter is given by the vector

$$\vec{N} = 0.5\left(\frac{\vec{R}_T}{R_T} + \frac{\vec{R}_R}{R_R}\right) \tag{2.3.1}$$

The tangency condition for the specular forward scatter can be expressed as

$$\vec{N} \cdot \vec{T} = 0 \tag{2.3.2}$$

This is the general framework that can be used as the starting point to analyze various conditions. Let's consider the Cartesian system in Fig. (2.2.1) and assume that a trail has occurred in the YZ plane. The angle between the trail axis and the wind planes is assumed to be 90 degrees, and we can express $\vec{T}$ as

$$\vec{T} = \hat{a}_y + \dot{v}(l)t\hat{a}_z \tag{2.3.3}$$

where $\dot{v}(l)$ is the derivative of v with respect to l, and $\dot{v}(l)t$ is the time varying slope of the distorted trail. $v(l)$ and $\dot{v}(l)$ are the wind profile and wind gradient along the trail. Equations (2.3.1-3), and (2.2.1-2) are combined to yield the following simplified condition

$$\dot{v}(l) = -\frac{y}{(zt)} \tag{2.3.4}$$

where y and z are coordinates of various points on the trail.

Here, we initially reconstruct Manning's work [6]. The meteor trail and the radar are both in a plane (YZ plane) composed of perpendicular bisectors of the transmitter-receiver base line. The radar point overlaps with the base line's midpoint. It is assumed that the wind distortion in the trail-radar plane is at right angles to the trail, either directed towards or away from the radar. The magnitude of the displacement is correspondingly reduced by cosine of the zenith angle η of the meteor radiant. η is also called the trail elevation angle. We derive the mathematical tangency condition for the **back-scatter (radar)** case. The geometry is shown in Fig. 2.2.1. In this case z represents the radar-curvature line. The normal vector at point P can be expressed as

$$\vec{N} = y\hat{a}_y + z\hat{a}_z \tag{2.3.5}$$

and

$$\vec{T} = \Delta(y)\hat{a}_y + \Delta(z)\hat{a}_z = \Delta(y)\hat{a}_y + \Delta(v)t\hat{a}_z \tag{2.3.6}$$

setting the dot product of the vectors $\vec{N}$ and $\vec{T}$ equal to zero results in

$$\frac{(\Delta v)}{(\Delta y)} = \dot{v}(l) = -\frac{y}{(zt)} \tag{2.3.7}$$

which is the same as Eq. (2.3.4). This **equivalence** allows us to utilize the back-scatter model (Fig.2.3.1) to investigate various conditions. The results can then be applied to oblique propagation with little need for modification.

2.4 SIMULATION MODEL

In this section, we formulate an approach to solve the following problem: Given a typical wind profile which distorts the trail, which points on the trail will scatter as a function of time? A point (y,z) on the trail is called a scattering point (glint) if it satisfies the condition in equation (2.2.7). Therefore, the study of trail distortion, glint generating mechanisms and their effect on meteoric signals involves solving this stochastic-differential equation in which $\dot{v}(l)$ is a gaussian random process.

Wind profiles are assumed to be band-limited gaussian processes. The number of samples needed to construct the process on the computer are $2BL$, where L is the length of the trail and B is the bandwidth of the process in cycles/km. Several different wind profiles were used in the computer-generated simulation model [Fig. 2.4.1]. $2BL$ points [v(1),v(2),...v($2BL$)] were generated by a gaussian random generator. The resulting $20BL$ point data sequence was then differentiated. The output sequence is the wind gradient $[\dot{v}(1), \dot{v}(2), \ldots, \dot{v}(20BL)]$. Rather than checking the equality in equation (2.2.4), we plot $m = \dot{v}(l) - y/(zt)$ versus y. The zero-crossings of m are the scattering points (the block labeled "zero-crossing detector" in Fig. 2.4.1). z is taken to be the radar-curvature line (R). The geometry is illustrated in Fig.2.1.2. The trail's midpoint is located at (0,0), which is the initial scattering point.

Figure 2.4.1: The simulation Block Diagram

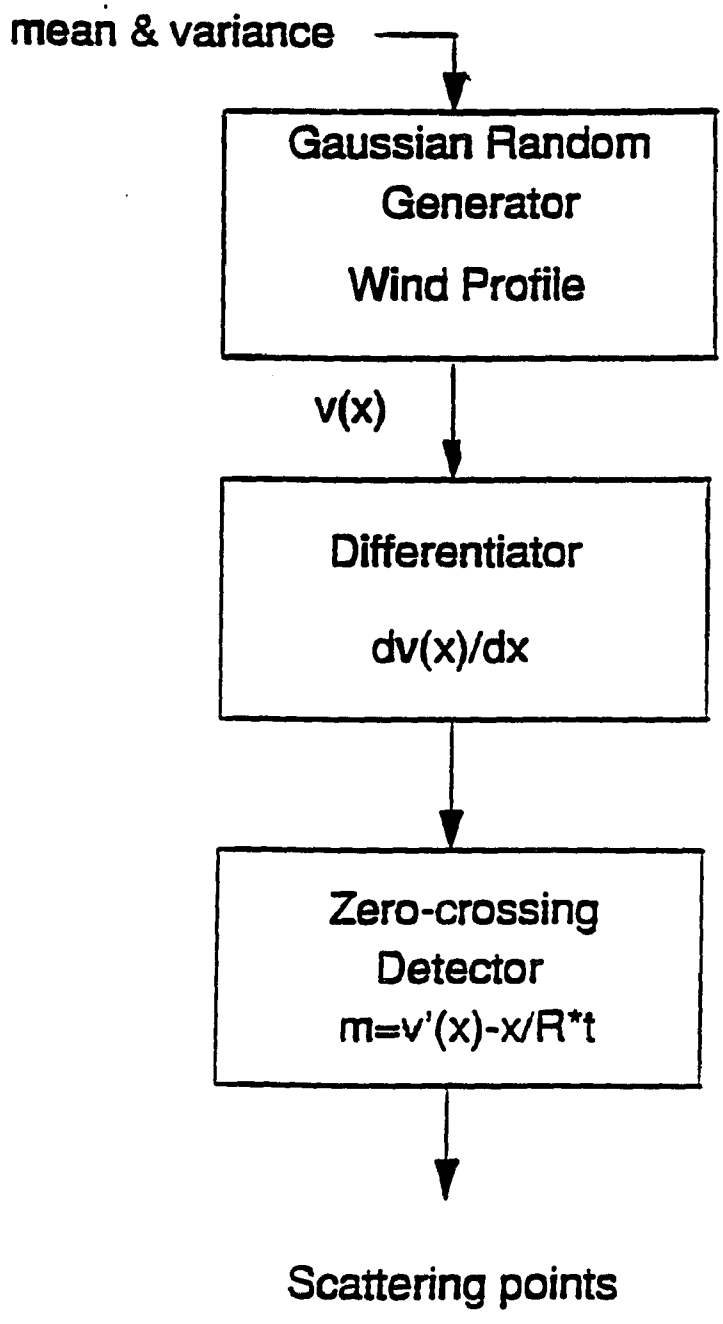

2.5 MULTIPATH SPREAD

Manning [6] showed that the energy scattering elements, or the 'trail aperture' as it may be called, is a gaussian function of the trail length centered about the initial perpendicular reflection point. The probability of finding energy scattered distant from the initial specular point, is reduced in accordance with the gaussian function, but the width of the distribution along the length of the trail increases linearly with time but it is ultimately limited by the trail length itself. This concept helps us gain insight into the multipath structure of the MB channel. Referring to equation (2.3.4), we set the trail aperture=y and R=z. Since $\dot{v}(l)$ is a gaussian random variable, y is also a gaussian process with mean

$$\overline{y} = \overline{\dot{v}} R t \tag{2.5.1}$$

This formula shows the linear growth of the aperture.

Figure 2.5.1 illustrates the geometry of forward scatter involved in the calculation of f, the length of one-half of the first Fresnel zone. It is taken directly from [4] where the derivation for f is given. For f to be one-half the first Fresnel zone the following condition must be met:

$$R'_1 + R'_2 = R_1 + R_2 + \frac{\lambda}{2} \tag{2.5.2}$$

It is shown that [4]

$$f = \sqrt{\frac{[\lambda R_1 R_2]}{[(R_1 + R_2)\sin^2 \omega]}} \tag{2.5.3}$$

This formula can be applied to the following condition:

$$R'_1 + R'_2 = R_1 + R_2 + \delta R \tag{2.5.4}$$

The zone on the trail is now the gaussian aperture (y=f). Equations (1),(2) & (3) are combined to solve for δR

$$\tau = \frac{(\delta R)}{c} = \frac{((R_1 + R_2)y^2 \sin^2 \omega)}{(4R_1R_2c)} \qquad (2.5.4)$$

where τ is the multipath spread and c is the speed of light. Equation (2.5.4) shows that the delay spread is a function of the length of the trail aperture and the link geometry. **The new delay spread formula [Eq. 2.5.4] is derived on the basis of Manning's glint theory. It successfully provides a physical insight into the delay spread mechanism due to wind-induced trail distortion.**

Figure 2.5.1: The geometry involved in the calculation of f [4]

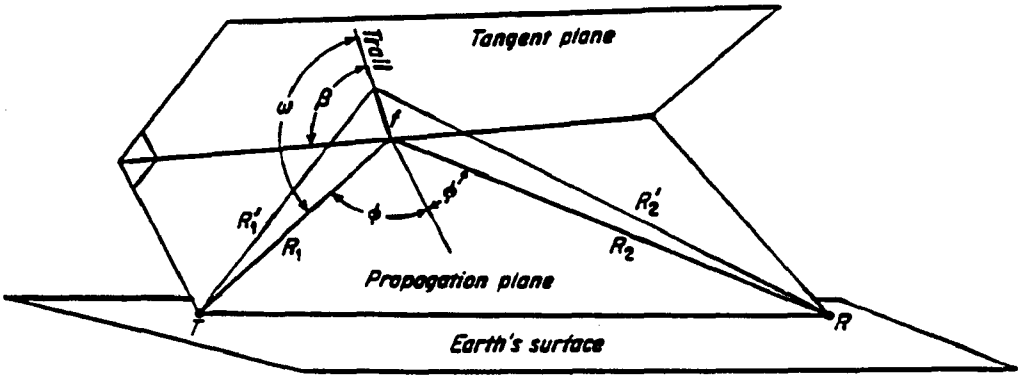

3 METEOR BURST PHASE PERTURBATIONS

3.1 DOPPLER RATE

The simulation model described in the previous chapter was used to study the trail distortion caused by various wind profiles. The trail distortion process is shown for three various wind profiles in Figures 3.1.1-3. The wind profiles have different bandwidth; this results in some trails having more peaks and valleys than others. Bandwidth is defined as the number of cycles per kilometer. Various wind profiles were used in the simulation model. For the underdense trails, the point of interest is the behavior of the single scatterer. As time advances, the original specular reflection point shifts its position along the trail, and hence is subjected to different wind velocities at various heights. This results in a linear change of the doppler shift, termed the doppler rate, as illustrated in figures 3.1.5-6. The horizontal axis is the trail axis, and in each snapshot the location corresponding to m=0 is the glint's location. In the time interval [0.0,.25], the glint moves from x=0 km to x=-2 km. These points (x=0,x=-2 km) are subjected to wind velocities of -45 and 30 m/sec respectively (see figure 3.1.4, points a and b). With respect to overdense trails, which last up to a few seconds, we are interested in observing the birth of new scatterers as time advances. This will lead to the characterization of fading and the fading bandwidth [6]. We next characterize the doppler rate analytically to verify the above-mentioned simulation results. One important observation is that the original specular point moves along the gaussian curve until it reaches a peak or valley. We can take any curve segment in figures 3.1.1-4 and find the corresponding doppler rate. In general, the point moves $y_{max} = 1/2B$ km in a time $t_{max} = 1/2Bz\dot{v}(l)$ seconds. The corresponding wind acceleration is

$$a = \frac{(\Delta v)}{(\Delta t)} = \dot{v}(l)\frac{y_{max}}{(t_{max})} = \dot{v}^2(l)z \qquad (3.1.1)$$

The resulting doppler rate will be

$$\dot{f}_{w_{max}} = \dot{v}^2(l)\frac{z}{\lambda} \tag{3.1.2}$$

As an example, for z=150 km, $\lambda = 6m$, $\dot{v}(l) = .05m/\sec/m$, the maximum possible doppler rate will be 62.5 Hz/sec, which only lasts for .266 sec. (B=.25 cycles /km). The trail position and the link distance affect the doppler rate in the same way as the doppler shift. **The newly characterized MB doppler rate imposes a lower limit on the bandwidth of the carrier recovery circuits in the coherent receivers. This implies the existence of an irreducible error floor produced by this element of the MB phase perturbations.**

Figure 3.1.1: Bandwidth=.5 cycles /km and $\sigma_\psi = 110 m/\sec/km$

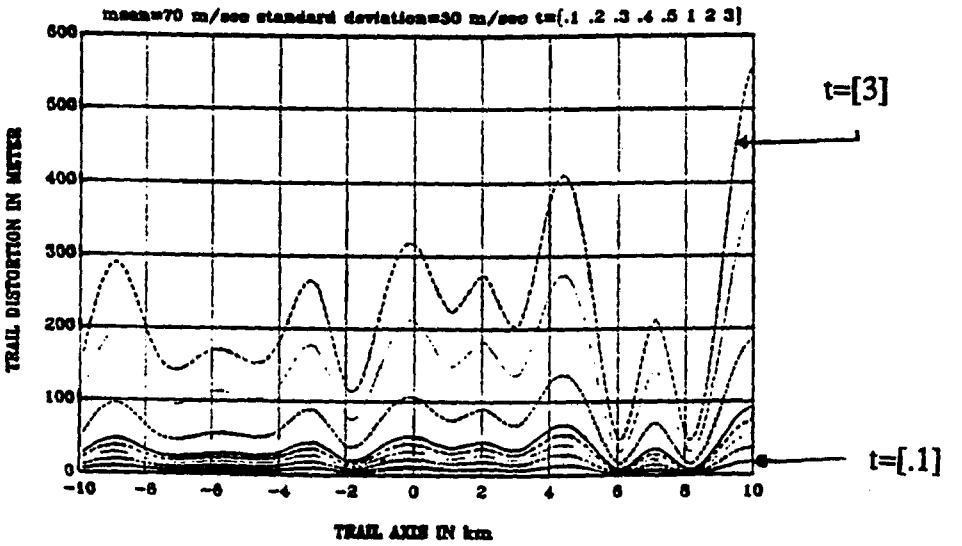

Figure 3.1.2: Bandwidth=.25 cycles/km and $\sigma_\psi = 40 m/\sec/km$

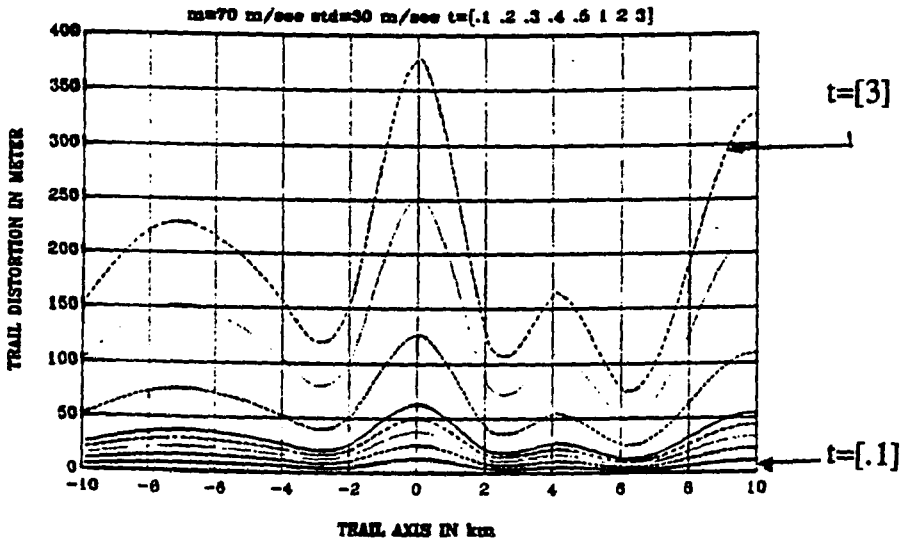

Figure 3.1.3: Bandwidth=.125 cycles/km $\sigma_\phi = 33.6 m/\sec/km$

t=[.1 .2 .3 .4 .5 1 2 3]

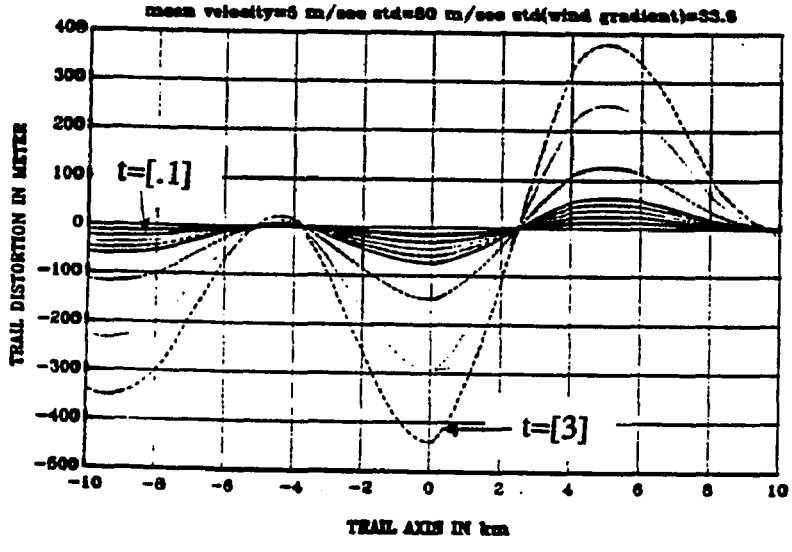

Figure 3.1.4: B=.25 cycles per km.

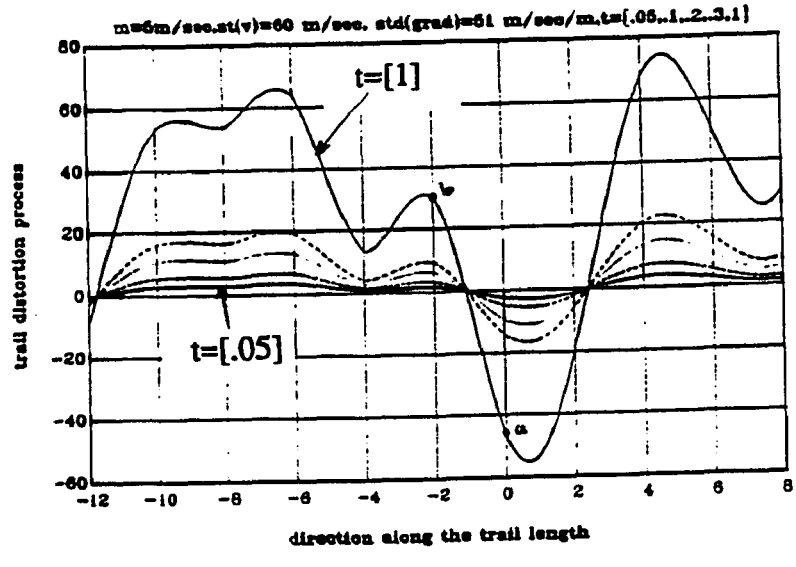

Figure 3.1.5: The Simulation Results

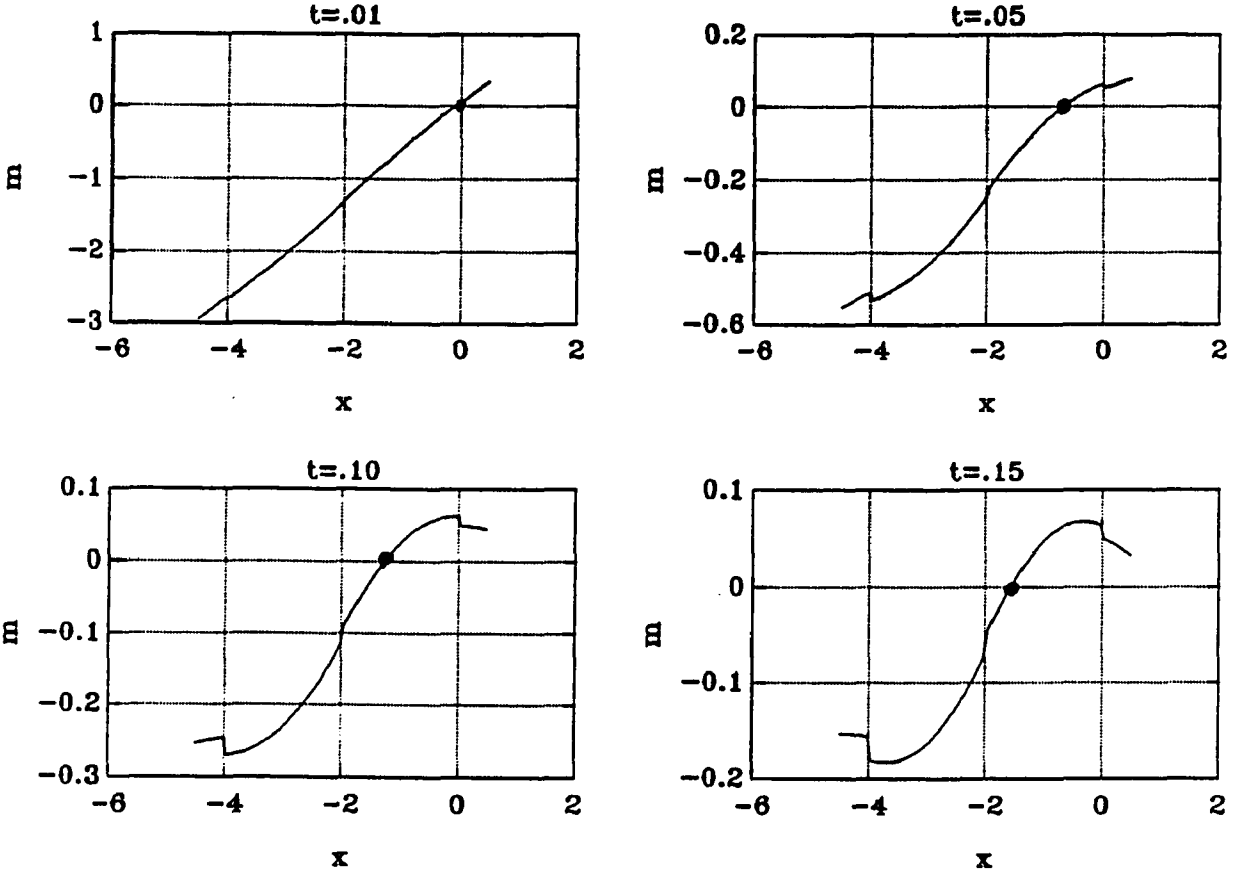

Figure 3.1.6: The Simulation Results

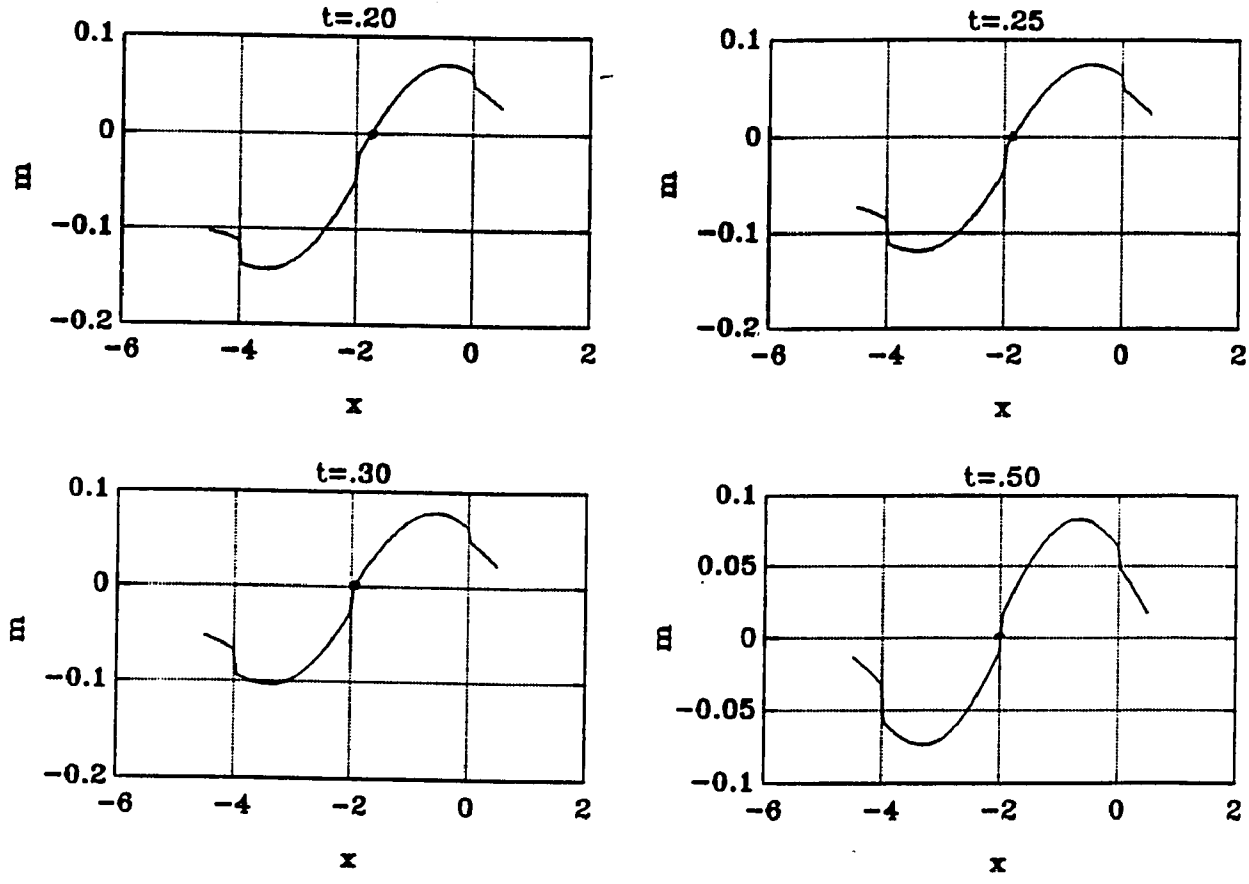

3.2 HEAD-ECHO PHASE JITTER

As first postulated by Herlofson, and carried out by Ellyet and Davies [53] at Jodrell Bank, meteor velocities can be measured by observing echo-amplitude fluctuations. Figure 3.2.1 provides amplitude-time radar record of meteor echo observed at Jodrell Bank by Davies [4]. The theoretical analysis of the diffraction echo phenomena is given in [4], however, the development is tailored to meteor velocity measurement applications. The frequency of the amplitude fluctuations is given by [4]

$$f_D = 2V^2 \frac{\tau}{R_0 \lambda} \tag{3.2.1}$$

The parameters will be defined later. The phase change due to diffraction, $\phi_D(t)$, is not yet treated analytically, although 5° rms jitter is observed experimentally [9]. The rms is sampled over a collection of trails, rather than over the lifetime of a single trail. To derive $\phi_D(t)$, we employ Manning's "moving-ball" interference theory [54] , consider the two types of reflections that can be obtained from the ionization trails. The first type is due to the specular reflection. The "specular" signal $s_1(t)$ appears after the meteor passes t_0 (Figure 3.2.2). The second type is of a transient nature, which only exists during the formation of the trail. It results when a continuous wave impinges upon the head of the rapidly advancing column of ionization [55]. The "head-echo" signal $s_2(t)$ suffers a doppler shift in frequency before it passes the specular reflection point at time t_0. After t_0, both signals exist and interfere. Therefore, we could argue that in the formative stage of the trail, the MB channel or reflecting medium consists of a stationary and a moving point (Figure 3.2.2). The formation process lasts for $t_D = L/2V$ seconds of the meteor signal's lifetime.

In general, when N signals with amplitudes a_i and phases ψ_i are combined, the resultant phase and amplitude is readily shown to be

$$\psi_t = \tan^{-1} \frac{\left(\sum_{i=0}^{N} a_i \sin(\psi_i) \right)}{\sum_{i=0}^{N} a_i \cos(\psi_i)} \tag{3.2.2}$$

$$A_t = \sqrt{\left(\sum_{i=0}^{N} a_i \cos(\psi_i) \right)^2 + \left(\sum_{i=0}^{N} a_i \sin(\psi_i) \right)^2} \tag{3.2.3}$$

in the meteor back-scatter case, the two signals

$$s_1(t) = a \cos(\omega_c t) \tag{3.2.4}$$

and

$$s_2(t) = b \cos(\omega_c t + \omega_D t) \tag{3.2.5}$$

interfere and yield

$$\phi_D(t) = \tan^{-1} \frac{b \sin(\omega_D t)}{a + b \cos(\omega_D t)} \tag{3.2.6}$$

which can be approximated for small values of b/a as

$$\phi_D(t) \sim \left(\frac{b}{a} \right) \sin(\omega_D t) \quad \text{rad.} \tag{3.2.7}$$

The next step is to derive an expression for $\omega_D = 2\pi f_D$. Considering Fig. (3.2.2), we can see that

$$\frac{v_l}{v} = \cos(\pi/2 - \phi) = \sin(\phi) = S(t)/R_0 \tag{3.2.8}$$

and

$$v_l = f_D \frac{\lambda}{2} = v S(t)/R_0 \tag{3.2.9}$$

This leads to an expression equal to equation (3.2.1)

$$f_D = \frac{2V^2\tau}{R_0\lambda} \tag{3.2.10}$$

where $\tau = t - t_0$,V is the meteor velocity, and R_0 is the radar-reflection point distance.

The fact that the rms phase jitter is 5° = .089 rad., implies that b/a = .089, which confirms that the "head-echo" signal is much weaker than the "specular signal".

The last step is to extend the results to the forward scatter MB channel. The considerations for $\frac{b}{a}$ remain unchanged, since the relative strength of the two signals is independent of the link geometry. This not true for f_D.

The meteor and the moving cloud move with the velocity $\vec{V} = (V_x\vec{a}_x + V_y\vec{a}_y + V_z\vec{a}_z)$. The treatment described in section 2.2 can be applied to this case to derive an expression for f_D

$$f_D = \frac{(x-d)V_x + yV_y + zV_z}{\lambda\sqrt{(x-d)^2+y^2+z^2}} + \frac{(x+d)V_x + yV_y + zV_z}{\lambda\sqrt{(x+d)^2+y^2+z^2}} \tag{3.2.11}$$

where (x,y,z) is the coordinate of the moving point. **Equations 3.2.7 and 3.2.11 characterize the head-echo induced phase jitter.** Using equation 3.2.11, Fig. (3.2.3) is developed to demonstrate how f_D changes as a function of x for short-,mid-, and long-range links. **It can be seen that for all trail locations, f_D is greater than 1 kHz. At these frequencies, QPSK or MPSK signal would suffer sever degradation if the head-echo induced phase jitter is not compensated for.**

Figure 3.2.1: Diffraction echo-amplitude fluctuations (Courtesy of J.G. Davies.)

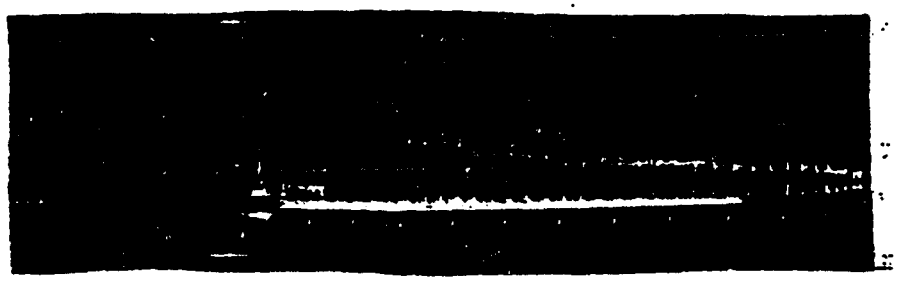

Figure 3.2.2: The interference model

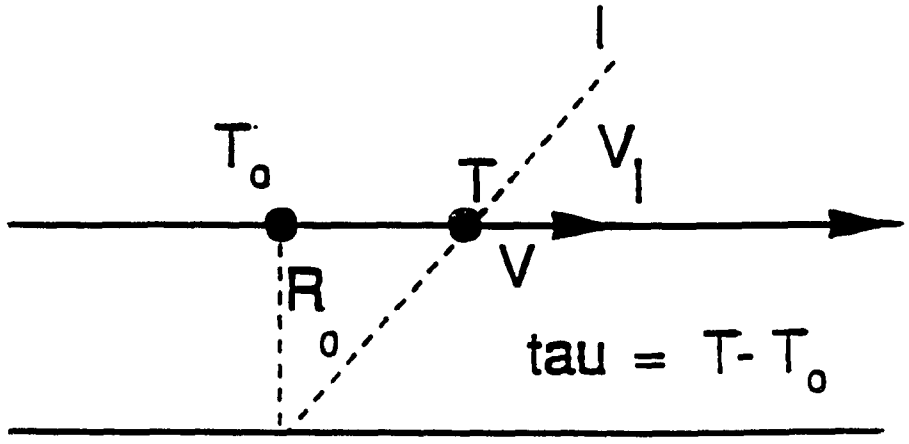

Figure 3.2.3: f_D vs. x ,and the link distance.

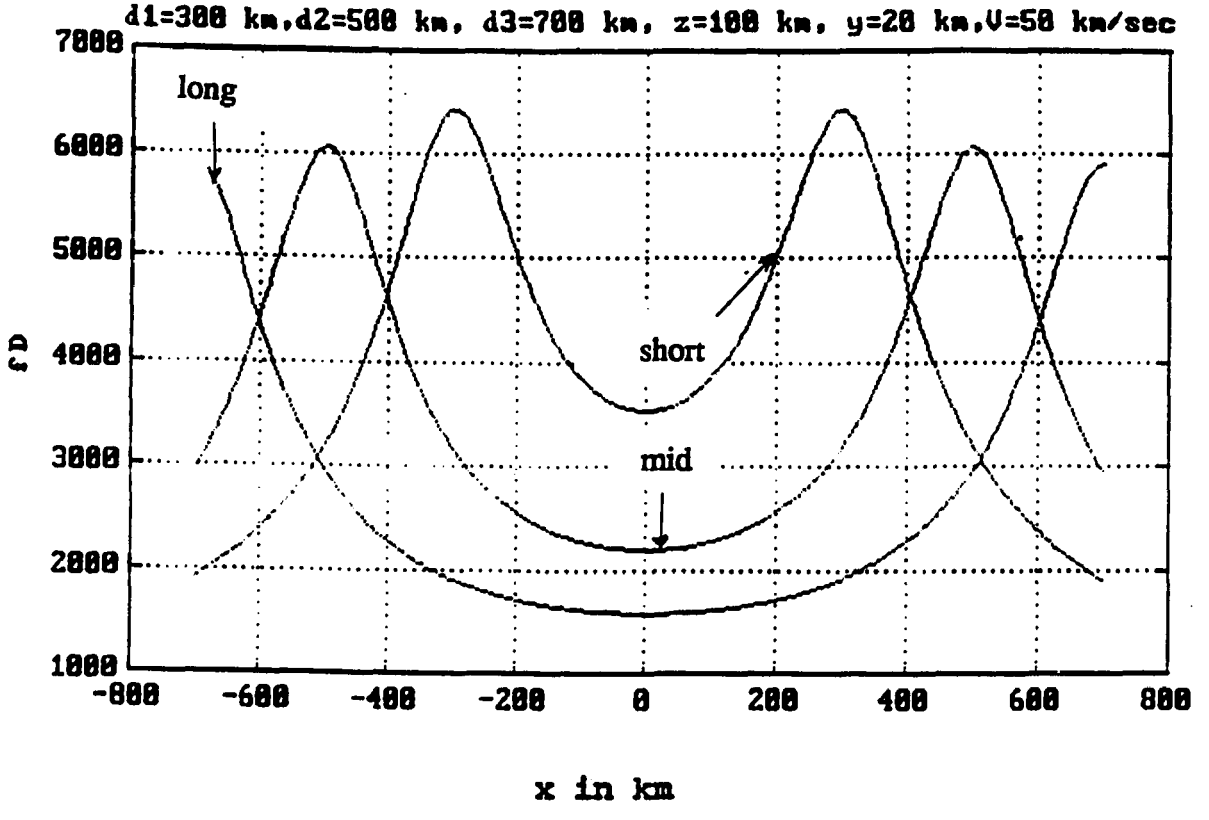

3.3 RESONANCE

When the electric vector in the incident radio wave is perpendicular to the ionized column, theory predicts a phase change of π radians during resonance. According to Kaiser 135 degrees of the change should occur before maximum, and 45 degrees after this point [11]. This is illustrated in Figure (3.3.1). Resonance is a transient process and only lasts for a time duration

$$t_R = \frac{\lambda^2 10^{-12} q}{16\pi^2 D} \tag{3.3.1}$$

where q is the electron line density and D is the diffusion rate.

A set of experimental results is given in [10]. Figure (3.3.2a) is a histogram of $\phi_R(t_R)$ resonance-induced phase changes measured after amplitude maxima. Figure (3.3.2b) is the distribution of the duration of the resonance (t_R), and Fig. (3.3.2c) charts the burst duration data in this experiment.

In the resonance time span, t_R, we can employ the linear approximation and express $\phi_R(t)$ as

$$\phi_R(t) = 2\pi f_R t\{u(t) - u(t - t_R)\} \tag{3.3.2}$$

where f_R is the doppler shift caused by this process. The step function is used to emphasize the transient nature of resonance. As an example, using the typical numbers $t_R = 13.3$ msec and $\phi_R(t_R) = \pi/3$ rad, we find an effective doppler shift of $f_R = 12.5$ Hz. In general, the resonance effect exists in the first 50 msec of the burst duration. In this time interval, resonance increases the phase error in an MPSK receiver and thus causes higher bit error probability.

Figure 3.3.1: Theoretical phase variation , for transverse scattering (after Kaiser [11])

$T = t_R, \alpha = q$ **and** $\phi = \phi_R(t) = 2\pi f_R t$

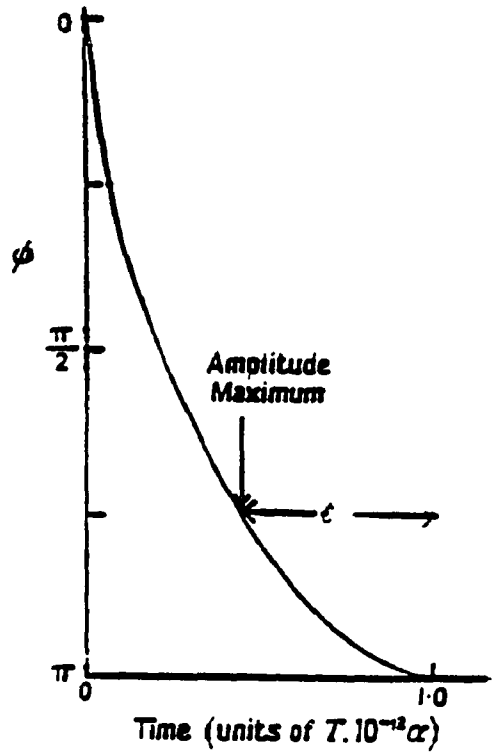

Figure 3.3.2: The set of experimental results (after Greenhow and Neufeld [10]) a: Histogram of the resonance-induced phase changes

b: Histogram of the resonance duration

c: Histogram of the burst duration

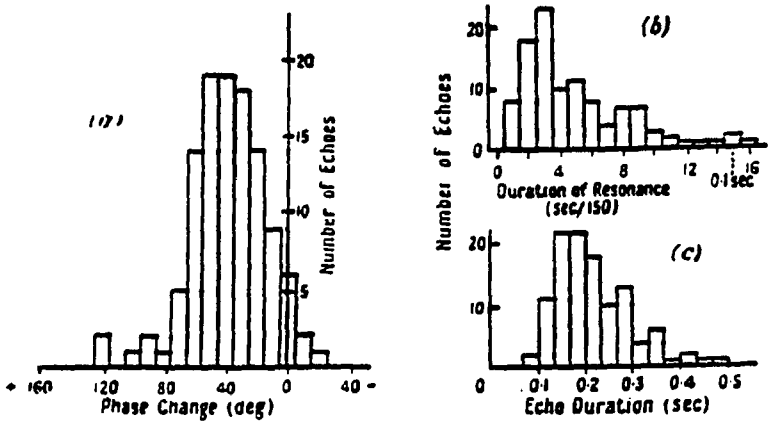

4 THE NEW CHANNEL MODEL

In this chapter we will present the general characteristics of the received meteoric signal s(t) which is defined as

$$s(t) = \sqrt{2P_s(t)}\cos[\omega_0 t + \phi_{MB}(t)] \tag{4.0.1}$$

where $P_s(t)$ is the received power as a function of time, which decays exponentially, and $\phi_{MB}(t)$ is the MB channel phase perturbation.

4.1 RECEIVED POWER AND AMPLITUDE

An underdense trail can be modeled as a cylindrical column of ions and electrons. One coherent waveform from a distant oscillator illuminates the trail. The incident radio wave penetrates the column and is scattered by individual free electrons, which oscillate freely in the applied field without colliding with other particles.

The wavelet scattered from any given electron is in phase with the adjacent wave, and the total scattered wave is the vector sum of many coherent and monochromatic wavelets. Destructive interference of waves originating from different phase planes cause the received signal power to decay exponentially. This model is widely accepted [5], and was originally used to derive the power formula:

$$P_s(t) = C_u q^2 e^{-t/\tau} \tag{4.1.1}$$

where $P_s(t)$ is the received power, q is the electron line density , τ is the decay constant , and t is the time measured from the formation of the trail. C_u is in the form:

$$C_u = \frac{G_T G_R \lambda^3 \sin(\alpha)^2 P_T \exp -8\pi^2 r_0^2/\lambda^2 \sec(\phi)^2}{16\pi^2 R_T R_R (R_T + R_R)[1 - \cos^2(\beta)\sin^2(\phi)]}$$

(4.1.2)

Where G_T and G_R are the power gains of the antennas, λ is the wavelength of the carrier in meters, r_c is the classical radius of the electron, α is the angle between the electric vector at the meteor trail and R_R, P_T is the transmitted power, R_T and R_R are distances of the transmitter and receiver, respectively, from the scattering point, β is the angle between the trail and the plane of R_R and R_T, ϕ is one half the included angle between R_T and R_R, and r_0 is the initial radius of the trail in meters. The average value of the decay constant is

$$\bar{\tau} = \frac{\lambda^2 \sec^2(\phi)}{32\pi^2 D} \tag{4.1.3}$$

where D is the diffusion rate.

The burst duration of the trail can be expressed as a function of the decay constant and the initial and minimum required electron line densities

$$t_B = \tau \ln\left(\frac{q}{q_{\min}}\right) \tag{4.1.4}$$

where $q_{\min}$ is the minimum required density to support a transmission with a specific modulation scheme. $q_{\min}$ can be expressed as:

$$q_{\min} = \sqrt{\frac{N_0 R\, erfc^{-1}(P_{bmax})}{C_u}} \tag{4.1.5}$$

where R is the bit rate and N_0 is the noise spectral density in W/Hz. Furthermore,

$$erfc^{-1}(P_{bmax}) = \left(\frac{E_b}{N_0}\right)_{req} = \gamma_{th} \tag{4.1.6}$$

where γ_{th} is the required signal to noise ratio to keep P_e below a given desired value.

4.2 RECEIVED MB PHASE

Drawing from chapter 3, we can express the MB phase as

$$\phi_{MB}(t) = \phi_R(t) + \phi_D(t) + \phi_W(t) \tag{4.2.1}$$

where, $\phi_W(t)$, is the wind-induced phase change and is equal to

$$\phi_W(t) = \int_0^t (2\pi(f_W + \dot{f}_W t))dt \tag{4.2.2}$$

Also $\phi_R(t)$ and $\phi_D(t)$ represent the resonance and diffraction-induced phase changes respectively. Substituting equations (3.2.7),(3.3.2), and (4.2.2) into (4.2.1) yields

$$\phi_{MB}(t) = 2\pi(f_R(u(t) - u(t - t_R)))t + 2\pi f_W t + \pi \dot{f}_W t^2 + \frac{b}{a}\sin(2\pi f_D t)(u(t) - u(t - t_D)) \tag{4.2.3}$$

Which can also be written as

$$\phi_{MB}(t) = \Omega_0 t + .5\Omega_1 t^2 + \frac{b}{a}\sin(2\pi f_D t)(u(t) - u(t - t_D)) \tag{4.2.4}$$

Ω_0, Ω_1, f_D, and $\frac{b}{a}$ are the parameters of interest in evaluating the performance of the carrier recovery and symbol recovery circuits in a coherent receiver. Figure 4.2.1 is a sample of MB phase perturbation in which the constant doppler shift is ignored. **Equation 4.2.4 includes the major contributions of this dissertation. This new formula permits waveform coding and design for the bandlimited MB channel to be systematically approached and resolved. The new channel model can function as a basis of comparison for the performance of various modulation-coding schemes.**

Figure 4.2.1: MB phase change

$f_D = 500Hz, f_R = 10Hz, f_W = 30Hz, \dot{f}_W = 50Hz/\text{sec}$, and $\frac{b}{a} = .15Rad. = 8.6°$

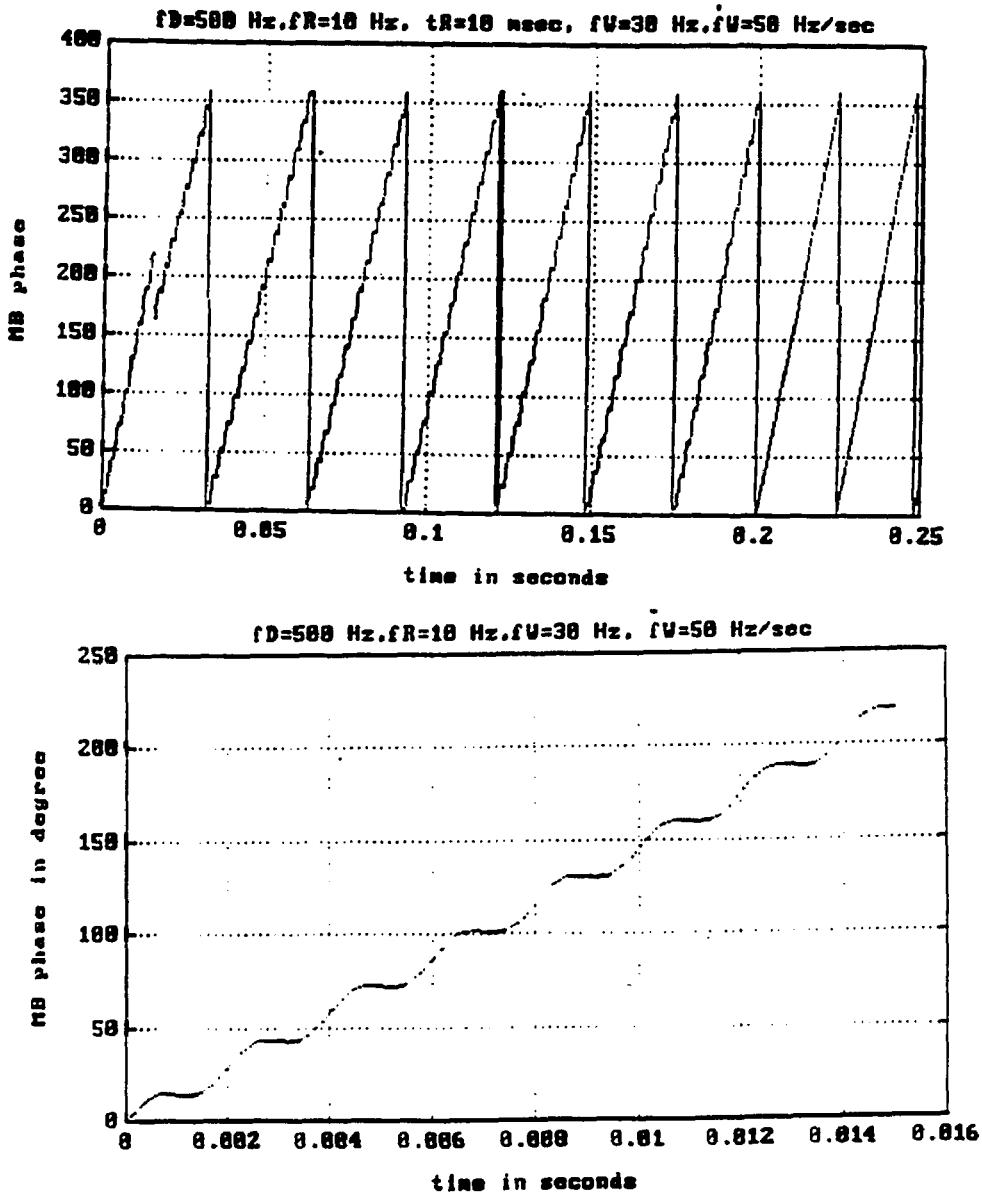

5 SYNCHRONIZATION

All coherent modulation schemes require initial phase and frequency acquisition , carrier recovery and timing recovery. A signal reflected from a meteor trail is subjected to phase distortions which were characterized in chapter 3. In this chapter, we will identify and isolate the relevant performance measures of a PLL carrier tracking loop needed to detect a received meteoric signal subjected to MB phase distortions.

5.1 ACQUISITION MODE PERFORMANCE MEASURES

Let us assume that the system enters the acquisition mode at $t = t_0$, that $\phi_{MB}(t)$ is the MB channel phase perturbation, and that $\hat{\phi}_{MB}(t)$ is the phase recovered by the loop. Under these assumptions we define, $\phi_{MB_e}(t) = \phi_{MB}(t) - \hat{\phi}_{MB}(t)$ as the phase error. Initially the phasors $\exp[i\phi_{MB}(t)]$ and $\exp[i\hat{\phi}_{MB}(t)]$ rotate at angular velocities ω and ω_0 Rad/sec, respectively, such that $\exp[i\phi_{MB}(t)]$ rotates at the rate $\Omega_0 = \omega - \omega_0$ rad/sec relative to $\exp[i\hat{\phi}_{Mb}(t)]$. The parameter $\Delta f = \frac{\Omega_0}{2\pi}$ is the initial frequency detuning, or the doppler offset in the system [12]. This is illustrated in Figure 5.1.1.

The synchronous mode is defined as the condition, $\dot{\phi}_{MB_e} \le \varepsilon_\Omega$ (frequency pull-in), and $\phi_{MB_e}(t) - 2n\pi \le \varepsilon_\phi$ (phase lock-in). Suppose that these conditions are first satisfied at $t = t_0 + t_{acq}$. The parameter t_{acq} is the signal acquisition time, since it represents the time required to reach the synchronous mode. Fig.5.1.2 illustrates the concepts of frequency pull-in, phase lock-in, and t_{acq}. Then from [13]

$$t_{acq} = T_P + T_L \tag{5.1.1}$$

where

$$T_L \sim \frac{2}{B_L} \tag{5.1.2}$$

and

$$T_P \sim \frac{4.2\Delta f^2}{B_L^3} \tag{5.1.3}$$

B_L is the one-sided bandwidth of the PLL, Δf is the doppler offset, T_P is the frequency pull-in time and T_L is the phase lock-in time.

Figure 5.1.1: Vector diagram illustrating the signal phasors (After Lindsey and Chie [12])

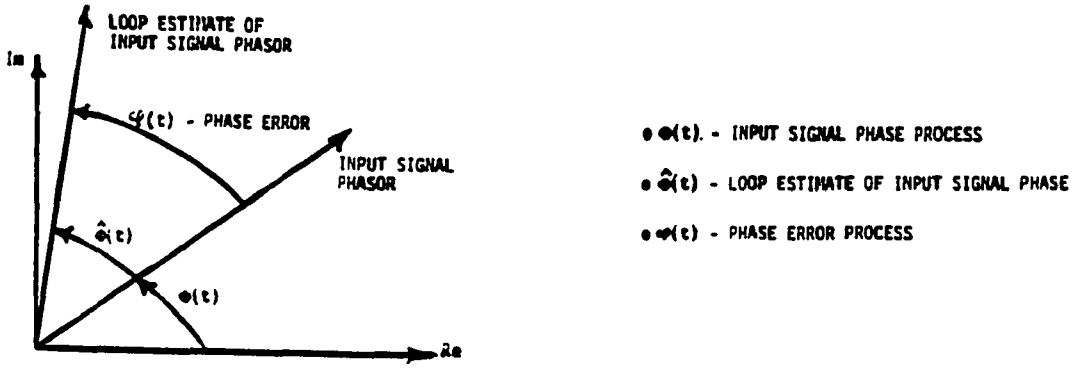

Figure 5.1.2: Frequency pull-in and phase lock-in [12]

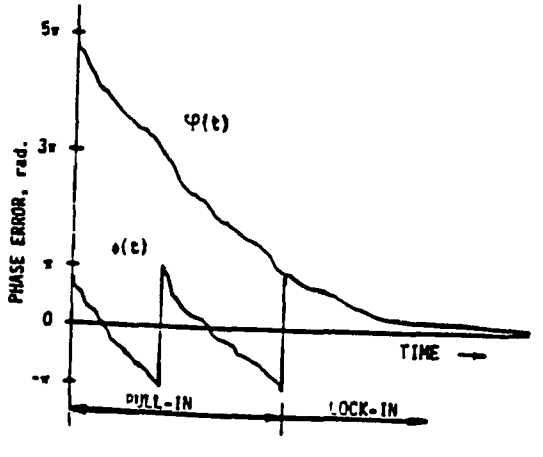

5.2 TRACKING MODE PERFORMANCE MEASURES

When the loop estimates the frequency and phase of the signal, two types of errors are encountered: the normal phase error jitter due to fluctuations of the loop estimate about its nominal value, and phase jumps by multiples of 2π radians (cycle slips). Statistical properties of the phase error jitter (rms error) determine the accuracy of the formation of the recovered signal, while measurement of the cycle slips determines the synchronization reliability. Basically, the cycle slipping rate S is required to determine the bit slippage probability, the loss-of-lock probability, and the probability of slipping a cycle in $[t_0,t]$. The cycle slipping phenomenon is shown in figure 5.2.1.

Given the density function of the phase error process is a function of ϕ and t ;$q(\phi,t)$, we find that $\psi(t)=\int_0^{\infty} q(\phi,t)d\phi$ gives the probability distribution of the time. Its derivative is therefore the density function of the time, and the expected time to reach ϕ_t for the first time is

$$E(T)=\int_0^{\infty} -t\dot{\psi}(t)dt \tag{5.2.1}$$

This approach was used by Viterbi [15] to derive the bounds for $T(2\pi)$ which is the expected cycle slipping time for the first order loop. The bounds of $T(2\pi)$ are

$$\exp(\pi\rho)/B_L < T(2\pi) < \pi\exp(2\rho)/(4B_L) \tag{5.2.2}$$

where ρ is the loop signal to noise ratio, and is equal to

$$\rho=\left(\frac{E_b}{N_0}\right)\left(\frac{f_b}{B_L}\right) \tag{5.2.3}$$

If we set a lock limit other than 2π --such as ϕ_t-- the average time to lose lock, $T(\phi_t)$, will equal to [15]

$$T(\phi_l) > \phi_l^2 \exp\frac{(2\rho)}{(16\pi B_L)} \tag{5.2.4}$$

This equation can be used to analyze the synchronization reliability of a typical MPSK receiver.

Figure 5.2.1: Cycle slipping (After Lindsey and Chie [13])

$T_{f_p} = T(2\pi)$

a: Phase error $\phi(t)$

b: Reduced phase error

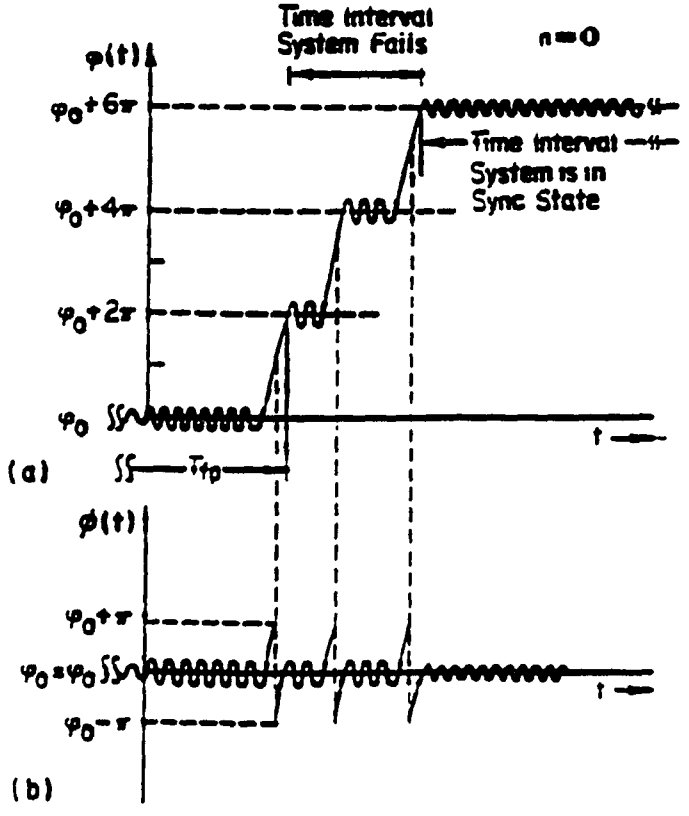

5.3 CARRIER TRACKING

In all applications pertaining to coherent telecommunications, it is necessary to reconstruct a carrier reference from a noise-corrupted version of the received signal.

For carrier tracking of a meteoric signal, the wind-induced doppler problem arises. Some second order phase locked loops are capable of tracking a constant doppler with negligible steady state error. However, derivatives of doppler such as the rate of change of the doppler can not be tracked. To accommodate these derivatives, the bandwidth of the loop must exceed a certain lower limit. On the other hand, the thermal noise rejection performance of the PLL is inversely proportional to its loop bandwidth.

We are interested in carrier recovery circuits used in MPSK modulation schemes. The reconstruction of a carrier for a polyphase signal can be accomplished in many ways. The simplest carrier synchronization system is the Mth power system shown in Figure 5.3.1. Lindsey and Simon gave a complete treatment of this problem and derived the formulae [16]

$$\sigma^2_{\phi_{th}} = S_L^{-1}/\rho \ \ rad. \tag{5.3.1}$$

and, for the RC bandpass filter,

$$S_L^{-1} = 1 + \sum_{r=0}^{M-2} \frac{(MC_r)^2}{M^2} \frac{((M-r-1)!2^{(M-r-1)})}{(2E_b/N_0)^{M-r-1}} \tag{5.3.2}$$

where S_L^{-1} is the squaring loss. By expanding the series, it is immediately seen that the terms corresponding to $r = M-2$ and $r = M-3$ constitute most of the overall sum. By doing so, equation (5.3.2) can be simplified to

$$S_L^{-1} = 1 + M\frac{(M-1)^2}{(4E_b/N_0)} + .66M(M-1)\frac{(M-2)}{(E_b/N_0)^2} \tag{5.3.3}$$

Substituting (5.3.3) in (5.3.1) results in

$$\sigma^2_{\phi_M} = \left(1 + M\frac{(M-1)^2}{(4E_b/N_0)} + .66M(M-1)\frac{(M-2)}{(E_b/N_0)^2}\right)\left(\frac{N_0}{E_b}\right)\left(\frac{B_{LM}}{f_b}\right) \tag{5.3.4}$$

where $B_{LM} = MB_L$ is the single-sided loop bandwidth for the PLL in a MPSK receiver structure (Fig. 5.3.1).

Figure 5.3.1: MPSK coherent receiver block diagram

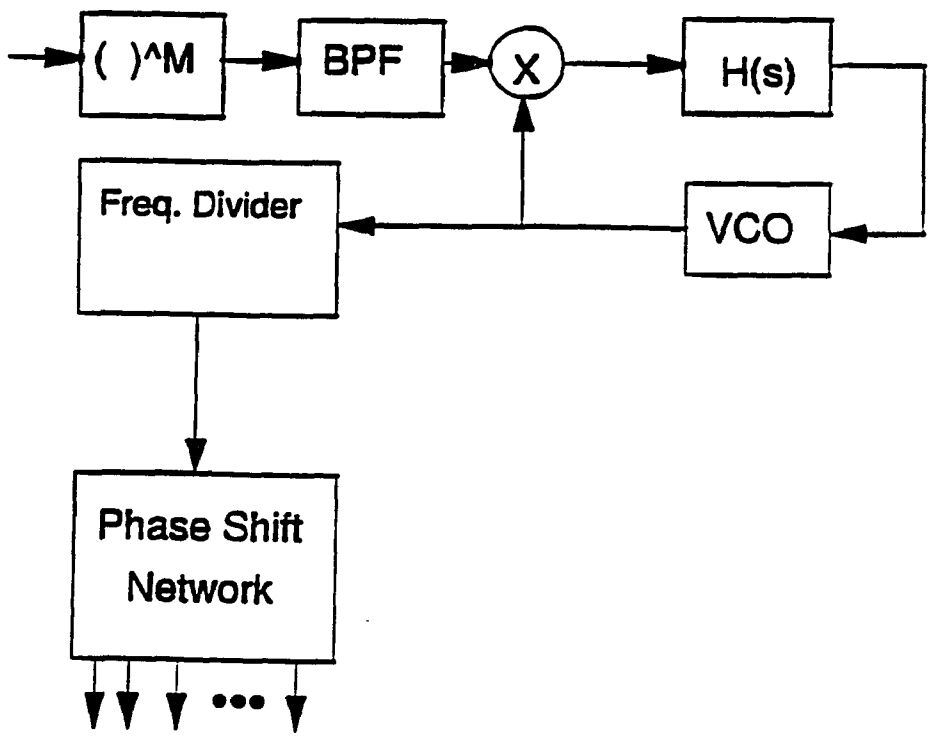

5.4 SYMBOL SYNCHRONIZER

A bit synchronizer designed to estimate the clock is a type of PLL. Symbol synchronization has to do with determining those instants in time when the modulation may change states. There are different types of bit synchronizers. Their main difference lies in the implementation of phase detector characteristics. An early-late gate synchronizer, which is very popular for rectangular pulses, is shown in figure (5.4.1). Gardner [13] analyzed this circuit and derived the following equation for the rms value of $\frac{(\Delta\tau)}{T}$ (the timing jitter):

$$\sigma^2_{\Delta\tau T} = \left(\frac{N_0}{(4d^2E_b)}\right)\left(\frac{B_{LS}}{f_b}\right) \tag{5.4.1}$$

where d is the transition probability, B_{LS} is the bandwidth of the symbol synchronizer , f_b is the bit rate and $\frac{E_b}{N_0}$ is the bit signal to noise ratio.

The time spread of a channel contributes to the timing uncertainty of the recovered clock, which is termed τ in figure (5.4.1). Also, the bandwidth of the symbol synchronizer is equal to

$$B_{LS} = \frac{1}{T_b} - \frac{1}{(T_b + \tau)} \tag{5.4.2}$$

The choice of a digital data format is also important. If we use a bi-phase data format , one transition per clock cycle is guaranteed. However, the bi-phase data stream occupies twice the spectrum than that occupied by the NRZ data stream, and therefore by choosing the bi-phase data format, we suffer a 3 dB loss in SNR.

Figure 5.4.1: Early-late gate synchronizer (After Gardner [13])

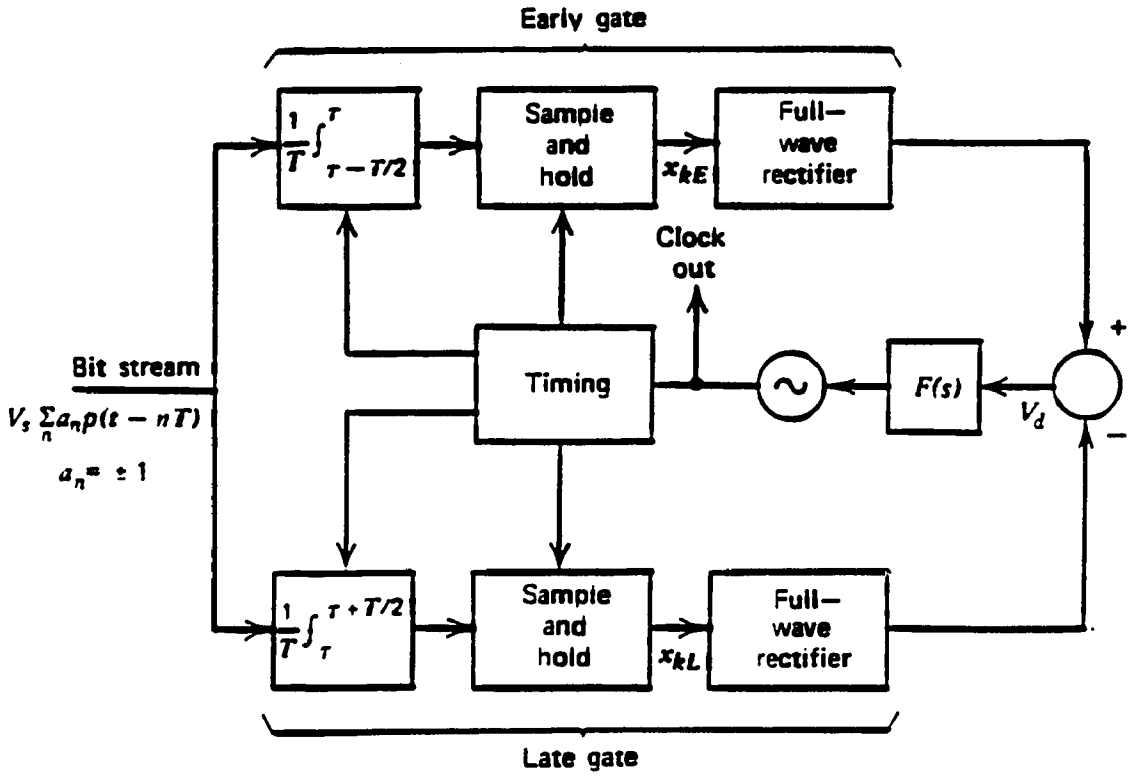

5.5 STEADY STATE AND TRANSIENT RESPONSE

The response of the loop to all kinds of phase perturbations such as phase step, frequency step, and frequency ramp needs to be identified. The steady state response to a frequency ramp is of particular interest. Since the burst duration is on the order of tenths of a second, the transient response duration is also of interest.

The steady-state response of the second-order loop to a phase step and a frequency step is zero. A third order loop is needed to force the steady state response to a frequency ramp towards zero; however, third order loops are highly unstable. The response of the second order loop to a frequency ramp (doppler rate) is [13]:

$$\phi_{s.s}(t) = \frac{\Omega_1}{\omega_n^2} \ rad \tag{5.5.1}$$

where $\omega_n = 1.9B_L$

The resonance effect vanishes after t_R seconds. This disappearance can be modelled as a step in frequency, requiring $t_{transient}$ seconds for the transient response to die away. The transient response of a second-order loop to a frequency step occurring in the time interval $[t_R, t_R + t_{transient}]$ is given by [13]

$$\phi_{R_e}(t) = 2\pi \frac{f_R}{\omega_n} \frac{\left(\sin\left(\sqrt{1-\xi^2}\,\omega_n t\right)\right)}{\left(\sqrt{1-\xi^2}\right)} \exp(-\xi\omega_n t) \tag{5.5.2}$$

Equation (5.5.2) is plotted in figure (5.5.1). In studying this curve we observe that for $\xi = .707, t_{transient} \sim 3/\omega_n$ seconds. During this time $\phi_{R_e}(t)$ can be modelled as a uniform random variable distributed between $(-\theta_1, \theta_1)$ where $\theta_1 = .5\frac{\Omega_0}{\omega_n}$, This yields

$$\sigma_{\phi_{R_e}} = 2\pi \frac{f_R}{(\omega_n\sqrt{3})} \ \text{rad} \tag{5.5.3}$$

The error response of the loop to the sinusoidal excitation $\phi_D(t) = \frac{b}{a}\sin(\omega_D t)$ is also sinusoidal. The magnitude of the phase error is simply the magnitude of the input phase multiplied by the magnitude response of the high pass filter (1-H(s)) with cutoff frequency B_L evaluated at the modulating frequency ω_D. At high modulating frequencies, the loop is unable to follow the modulation so that the full modulation phase appears as error at the phase detector.

Figure 5.5.1: Transient phase error $\theta_e(t) = \phi_{R_e}(t)$ due to a step in frequency $\Delta\omega = 2\pi f_R$ (From [13])

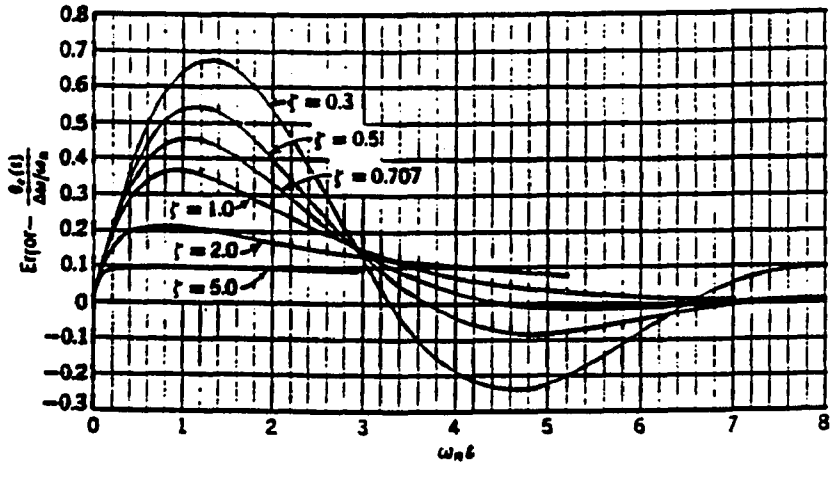

5.6 OPTIMUM LOOP BANDWIDTH

So far, we have characterized the MB phase process as

$$\phi_{MB}(t) = \Omega_0 t + .5\Omega_1 t^2 + \frac{b}{a}\sin(\omega_D t)\,(u(t) - u(t - t_D)) \tag{4.2.4}$$

The phase error, $\phi_{MB_e}(t)$, which is the response of the carrier recovery circuit to $\phi_{MB}(t)$ has been characterized. The phase error, which we term the MB phase jitter, is equal to

$$\phi_{MB_e}(t) = \frac{\Omega_1}{\omega_n^2} + n_R(t) + n_{th}(t) + A\frac{b}{a}\sin(\omega_D t) \tag{5.6.2}$$

The first term is the steady-state phase error expressed in radians due to $\dot{f}_W$, the wind-induced doppler rate. The second term, $n_R(t)$, is a uniform random process with mean zero and standard deviation $\sigma = \pi\frac{f_R}{(\omega_n\sqrt{(3)})}$ rad which exists in the time interval $[t_R, t_R + t_{transient}]$. The third term, $n_{th}(t)$, is the thermal noise-induced phase error process, which is a gaussian random variable with zero mean and variance, as given by equation (5.3.4); it is modulation-dependent. The fourth term is due to head-echo which exists only for $t_D = \frac{L}{(2V)}$ seconds. A depends on B_L and f_D. If f_D is greater than B_L, A will equal one, and the interfering signal will not be tracked.

The loop bandwidth B_L clearly emerges as the pivotal parameter. As considered in the previous section, the initial acquisition time t_{acq} also depends on B_L. As an example, we now determine the optimum value of B_L for the following typical conditions:

1) The maximum doppler spread is 30 Hz.

2) $f_R = 10$ Hz, $t_R = 15$ msec, $\dot{f}_W = 50$ Hz/sec, $t_W = .25$ sec, $f_D = 1000$ Hz, $b/a = 5°$.

3) Meteor velocity=50 km/sec, meteor length=L=20 km, $t_D = .2$ sec.

4) Channel bandwidth=40 kHz.

5) QPSK modulation, data rate= $f_b = 40$ kbps, $SNR = 10$ dB.

Figures (5.6.1a-b) represents samples of the MB phase jitter. Figures (5.6.2a-c) are histograms of phase jitter at three different time intervals of the trail's life-time. The first 20 msec. time interval (5.6.2a) represents the period during which resonance, thermal noise, and head-echo exist. In figure (5.6.2b), the resonance effect ceases to exist, and finally figure (5.6.2c) is the histogram of the phase jitter in the presence of thermal noise. The study of the three histograms reveals that the statistical properties of the phase jitter change as a function of time. The search for optimum loop bandwidth is simplified by only considering doppler rate and thermal noise in the analysis. This is justified by noting that the resonance effect only exists in the first 50 msec. of the trail's life-time, and that an adaptive equalizer can be built to nullify the head-echo effect. These results are illustrated in figures (5.6.3a-c) where phase jitter is plotted versus B_L under various operating conditions. These plots demonstrate that an optimum B_l exists which can be used in subsequent analysis.

The last figure (5.6.4) illustrates how t_{acq} changes as a function of B_L, where the initial doppler shift equals $\Delta(f) = 25Hz$.

Figure 5.6.1a: MB phase jitter, QPSK. [0-.05].

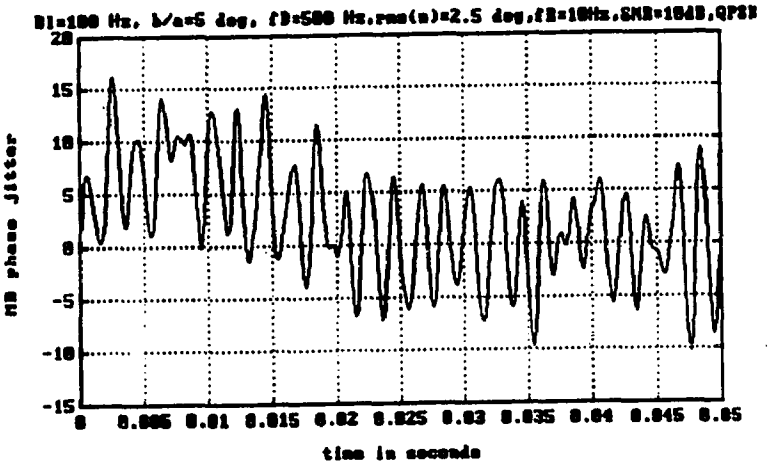

Figure 5.6.1b: MB phase jitter, QPSK. [.2-.25].

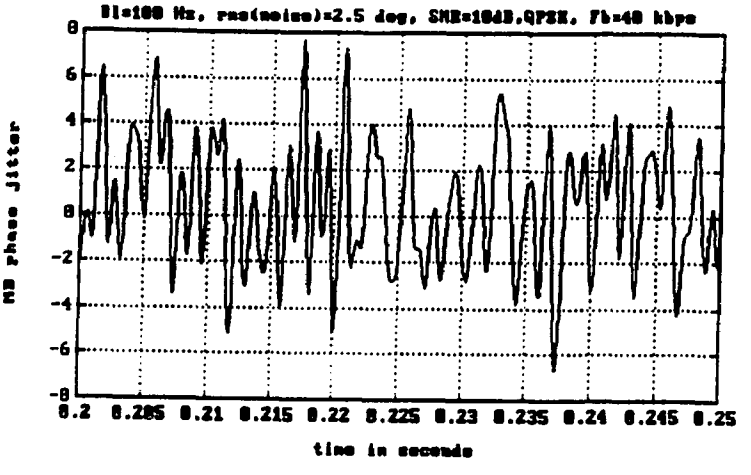

Figure 5.6.2a: [0-.02] seconds, the resonance's transient response, head-echo, doppler rate, thermal noise. Histogram of the phase jitter in the first 20 msec.

Figure 5.6.2b: [.02-.05] seconds, head-echo, doppler rate, thermal noise.

Figure 5.6.2c: [.2-.25] seconds, thermal noise.

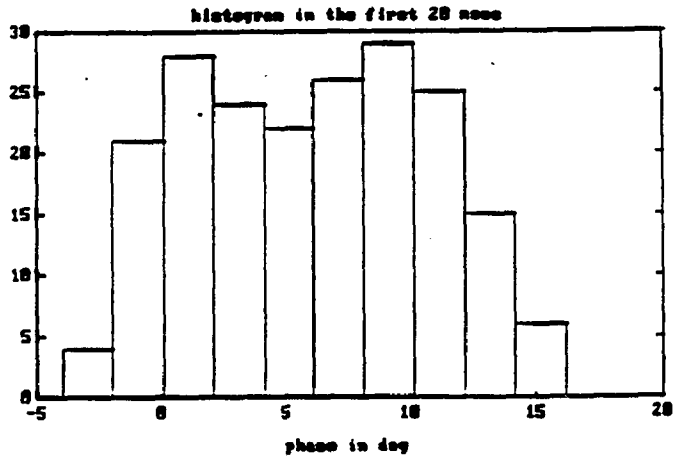

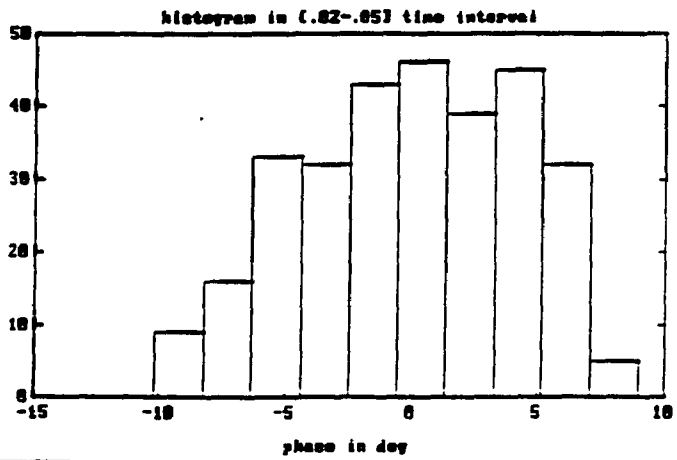

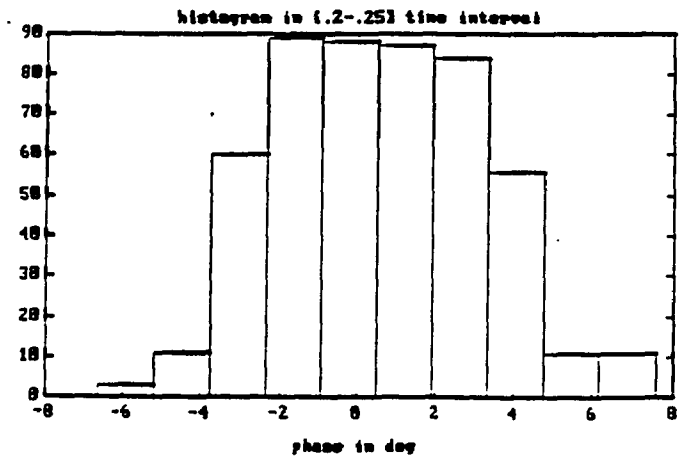

Figure 5.6.3a: rms phasor jitter vs. B_L, QPSK.

Figure 5.6.3b: 8PSK.

Figure 5.6.3c: 16PSK.

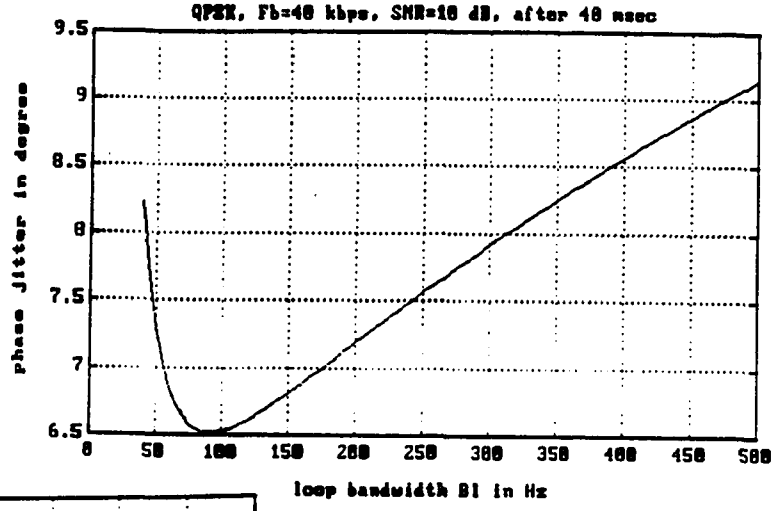

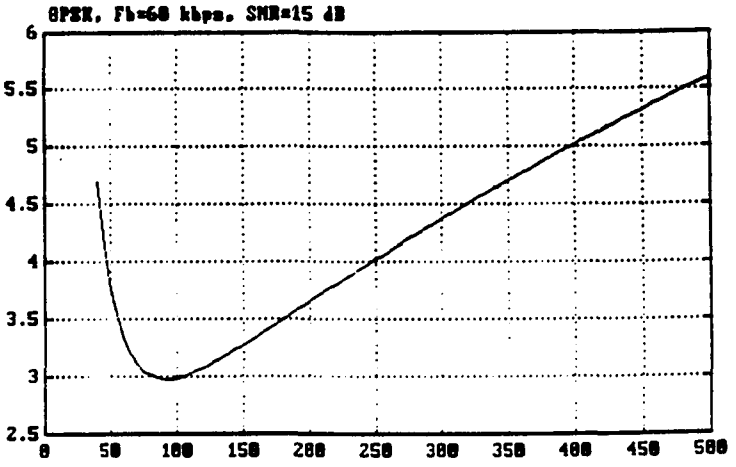

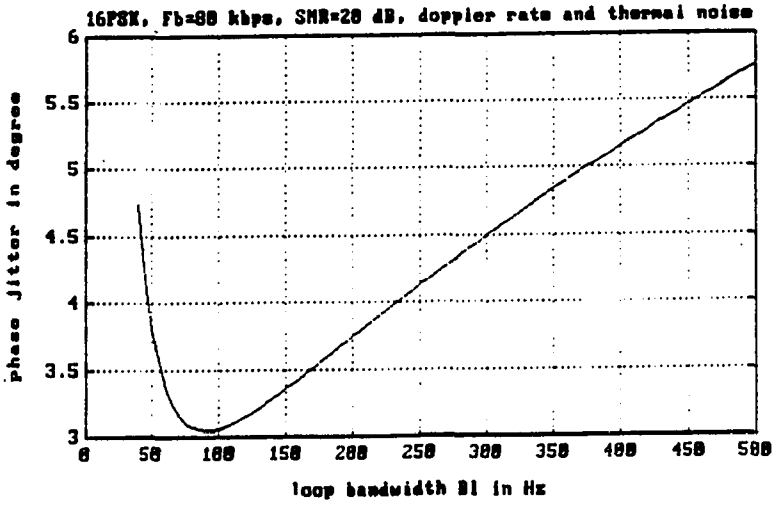

Figure 5.6.4: Acquisition time vs. B_L.

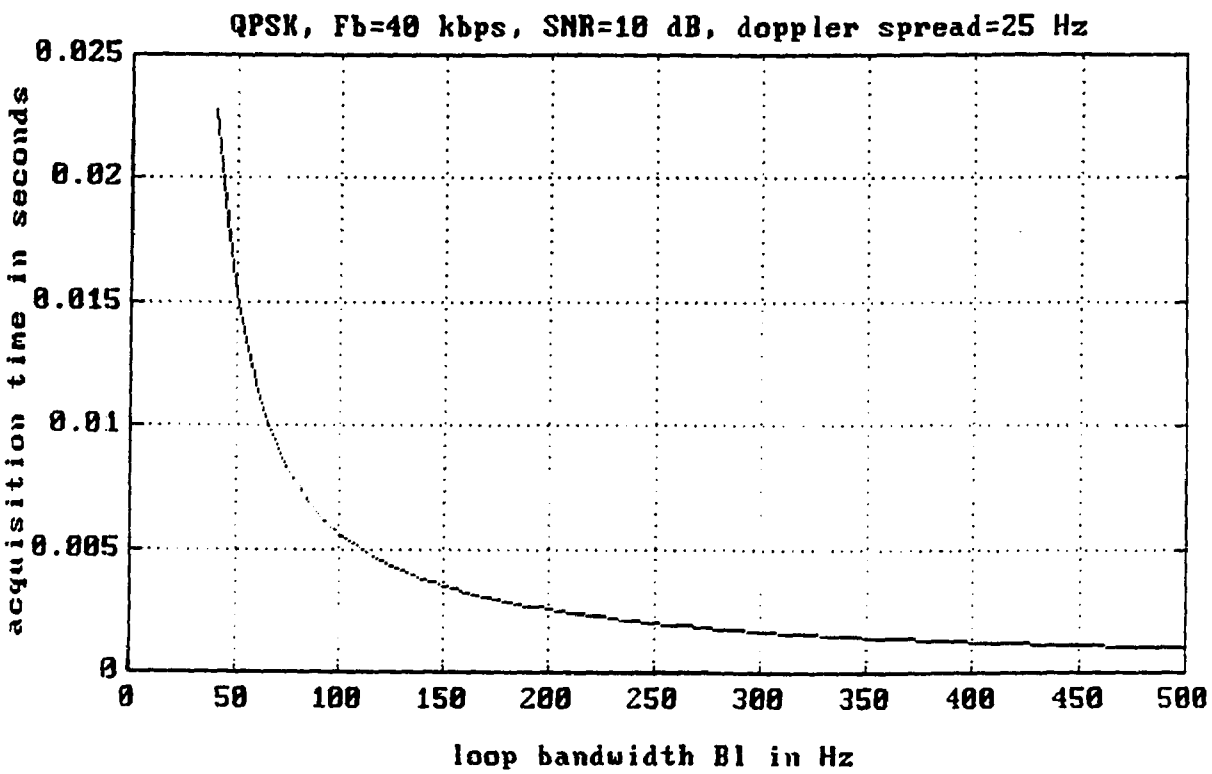

6 SYNCHRONIZATION LOSSES

In a recent paper, Jacobsmeyer [42] proposed a scheme called "adaptive trellis-coded modulation " for the band-limited MB channel. This work shows a throughput improvement by a factor of three. We will now describe this proposed modem. However, Jacobsmeyer did not incorporate the effect of the jitter losses in the performance evaluation. This chapter will formulate an approach in which the degradation due to MB phase changes are quantified.

Coherent modulation and channel coding schemes such as QAM, M-ary PSK , and Trellis coded M-ary PSK are bandwidth efficient and ideal at all SNRs. QAM can not be used for the MB Channel, since the high power non-linear amplifiers at the MB Master stations are not compatible with QAM. Trellis-coded modulation combines multilevel and/or multi-phase signaling with a finite state encoder to increase the distance between the signals without increasing the power. Typically, $M = 2^k$ signals are mapped into $2M = 2^{k+1}$ signals by using a convolutional encoder. The output of the encoder is then phase or amplitude modulated. Band-limitation of the MB Channel and the decrease in the received SNR as a function of time, suggest the use of an adaptive and spectrally efficient modem. The symbol size M, code rate, and the bit rate can all be varied as the received SNR decreases.

Figures (6.0.1-2) are block diagrams of a transmitter and a coherent receiver structure. The binary digits are trellis-coded and phase-modulated at the receiver. The received signal is first demodulated, and then decoded, by a Viterbi decoder. A detector is then used at the last signal processing stage (Fig. 6.0.2). Figure (6.0.3) illustrates how the adaptive coherent modem operates. t_{16} is the time-slot used to transmit data employing TC-16PSK. t_8 and t_4 correspond to TC-8PSK and TC-QPSK, respectively. The effects of the time and phase jitter are included in Figure (6.0.4). The shaded areas are due to initial synchronization time loss. A fixed-rate QPSK system is introduced

which will be used as a basis of comparison. Figures (6.0.5-6) illustrate the operation configuration of this system with and without the jitter losses. It must be noted that the use of each code rate will result in a different detection SNR threshold. Figure (6.0.7) shows the performance of the uncoded and coded QPSK modulation schemes.

The received trellis-coded MPSK signal is

$$r(t) = \sqrt{2P_s(t)}\cos[\omega_0 t + (2i-1)\pi/M + \phi_{MB}(t)] + n(t) \tag{6.0.1}$$

where $P_s(t)$, and $\phi_{MB}(t)$ are completely characterized using equations (4.1.1) and (4.2.3). Any "separation" of the transmitted sequence and the decoded sequence represents an error event. Such an event occurs whenever the received sequence is closer in the sense of Euclidean distance to some allowed sequence other than the transmitted one. The most likely errors occur between two sequences that are closest in terms of squared Euclidean distance. The minimum value of such is called the squared "free distance"

$$d_{free}^2 = \min_{\{a_n \neq b_n\}}(a_n - b_n)^2 \tag{6.0.2}$$

where

$$\{a_n\}, \{b_n\} \in C$$

If we denote the minimum distance between signals in the uncoded scheme as $d_{\min}$, the asymptotic coding gain of the TCM scheme is expressed as

$$G = 10\log(d_{free}^2/d_{\min}^2) \tag{6.0.3}$$

We define Δ to be the total jitter losses in dB, which is somewhat parallel to the concept of the coding gain,

$$\Delta = 10\log(d^2/d_j^2) \quad \text{dB} \tag{6.0.4}$$

The jitter loss formula can be simplified by focusing on the modulator/demodulator of the modem in figures (6.0.1-2). We assume that the recovered carrier signal is offset by $\phi_0 = rms(\phi_{MB_e}(t))$ degrees. Figure (6.0.8) illustrates how minimum distance of the MPSK signal constellation is effected by the phase offset. From the figure, d^2 can be found using

$$d^2 = 2E_s(1-\cos(2\pi/M)) = 2E_s(1-2\cos^2(\pi/M)+1) = 4NE_b\sin^2(\pi/M) \tag{6.0.5}$$

The ϕ_0 phase offset will change the distance. The new value will be $d^2_{PhaseJitter}$ and is equal to

$$d^2_{PhaseJitter} = 2E_s(1-\cos(2\pi/M-2\phi_0)) = 4NE_b\sin^2(\pi/M-\phi_0) \tag{6.0.6}$$

The timing offset by $\frac{\tau_0}{T} = rms\left(\frac{\tau}{T}\right)$ will further reduce the distance to

$$d_J^2 = 4NE_b\sin^2(\pi/M-\phi_0)\left(1-2\frac{\tau_0}{T}\right)^2 \tag{6.0.7}$$

Substituting equations (7) and (5) in (4) yields

$$\Delta = 10\log\left(\frac{\sin^2(\pi/M)}{\sin^2(\pi/M-\phi_0)(1-2\tau_0/T)^2}\right) \quad \text{dB} \tag{6.0.8}$$

where Δ is the total jitter loss in dB. Figures (6.0.9-11) illustrate how Δ changes as a function of SNR. This applies to three cases; TC-16PSK, TC-8PSK, and TC-QPSK. The detection threshold has to be extended to compensate for the penalty suffered due to synchronization jitter losses. That is, the SNR needed to maintain the bit probability of error below a constant value is now given by

$$\gamma_{new} = \gamma_{old} + \Delta \tag{6.0.9}$$

Figure 6.0.1: The adaptive coherent modem's transmitter

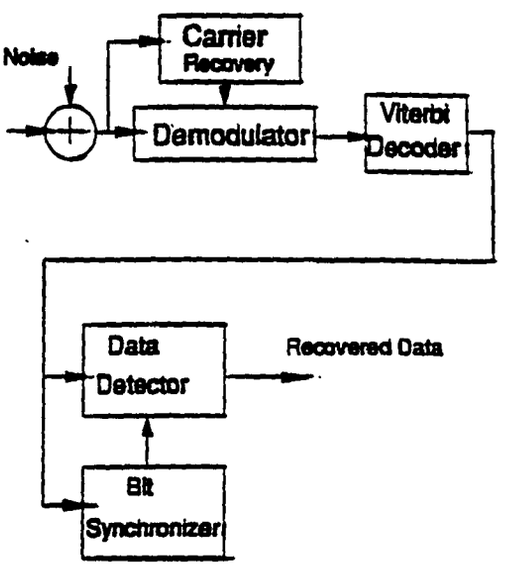

Figure 6.0.2: The adaptive coherent modem's receiver

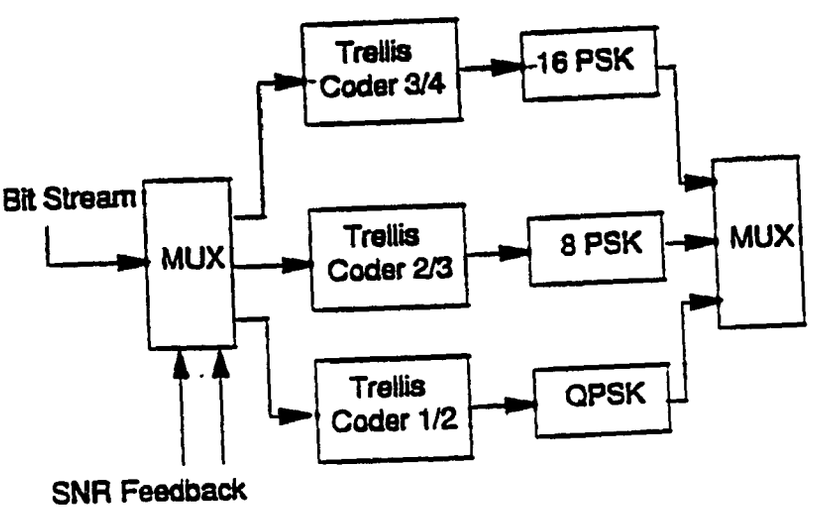

Figure 6.0.3: The operation principles of the adaptive coherent modem.

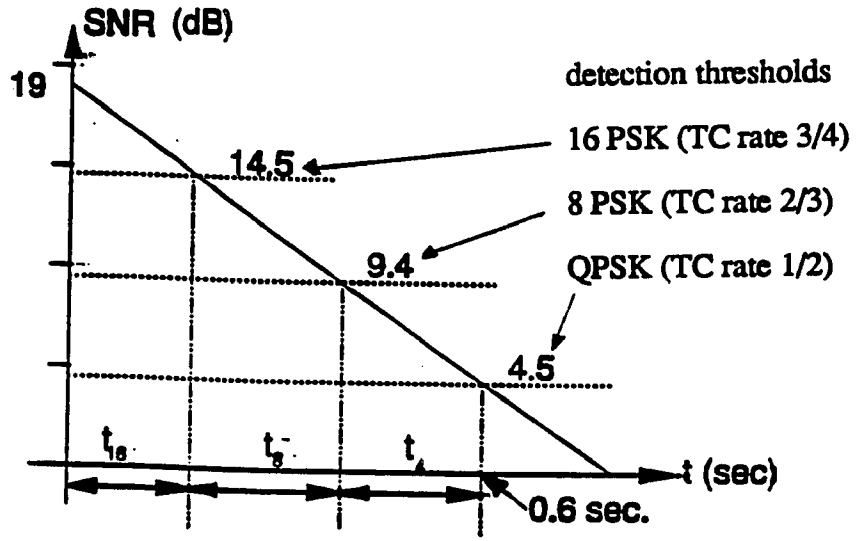

Figure 6.0.4: Jitter losses included.

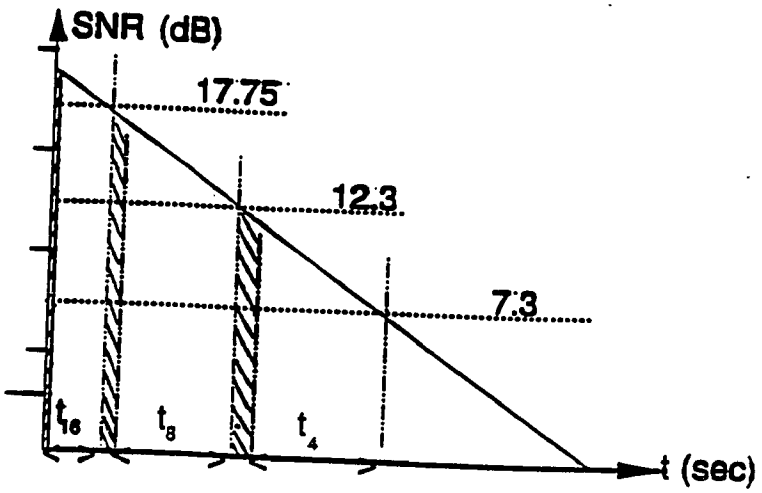

Figure 6.0.5: Fixed-rate QPSK.

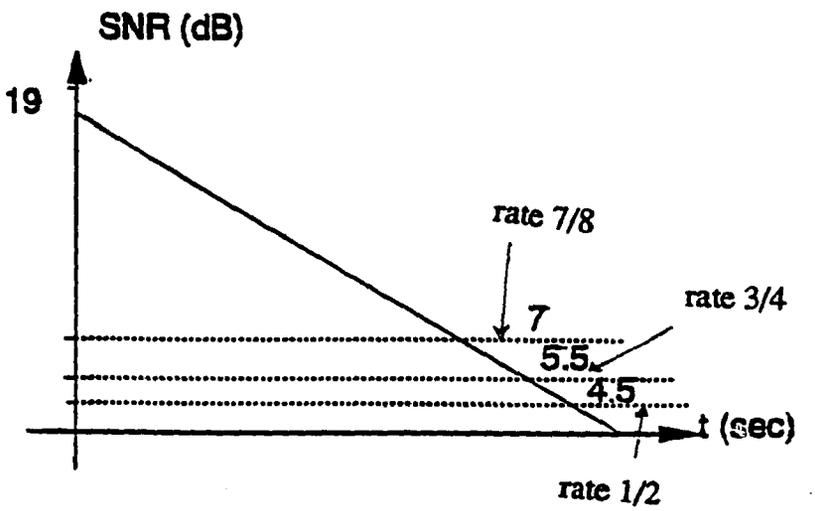

Figure 6.0.6: Fixed-rate QPSK with jitter losses.

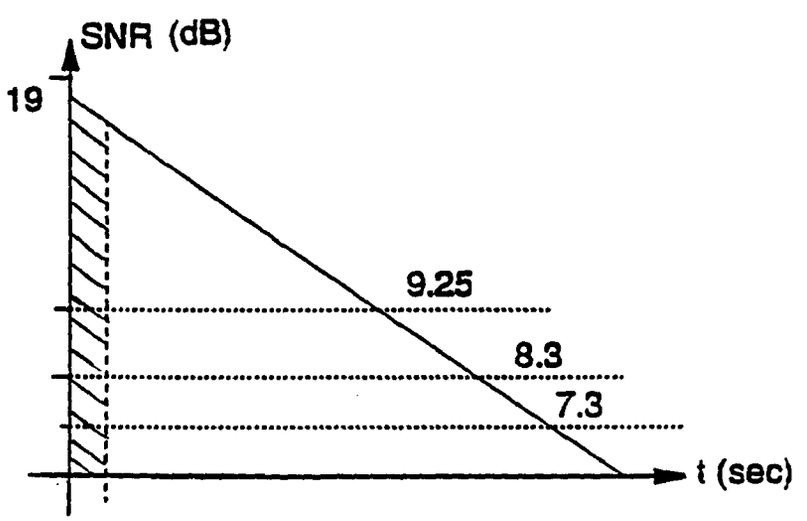

Figure 6.0.7: SNR vs. P_e, uncoded and coded QPSK,(courtesy of SCS Telecom Inc.)

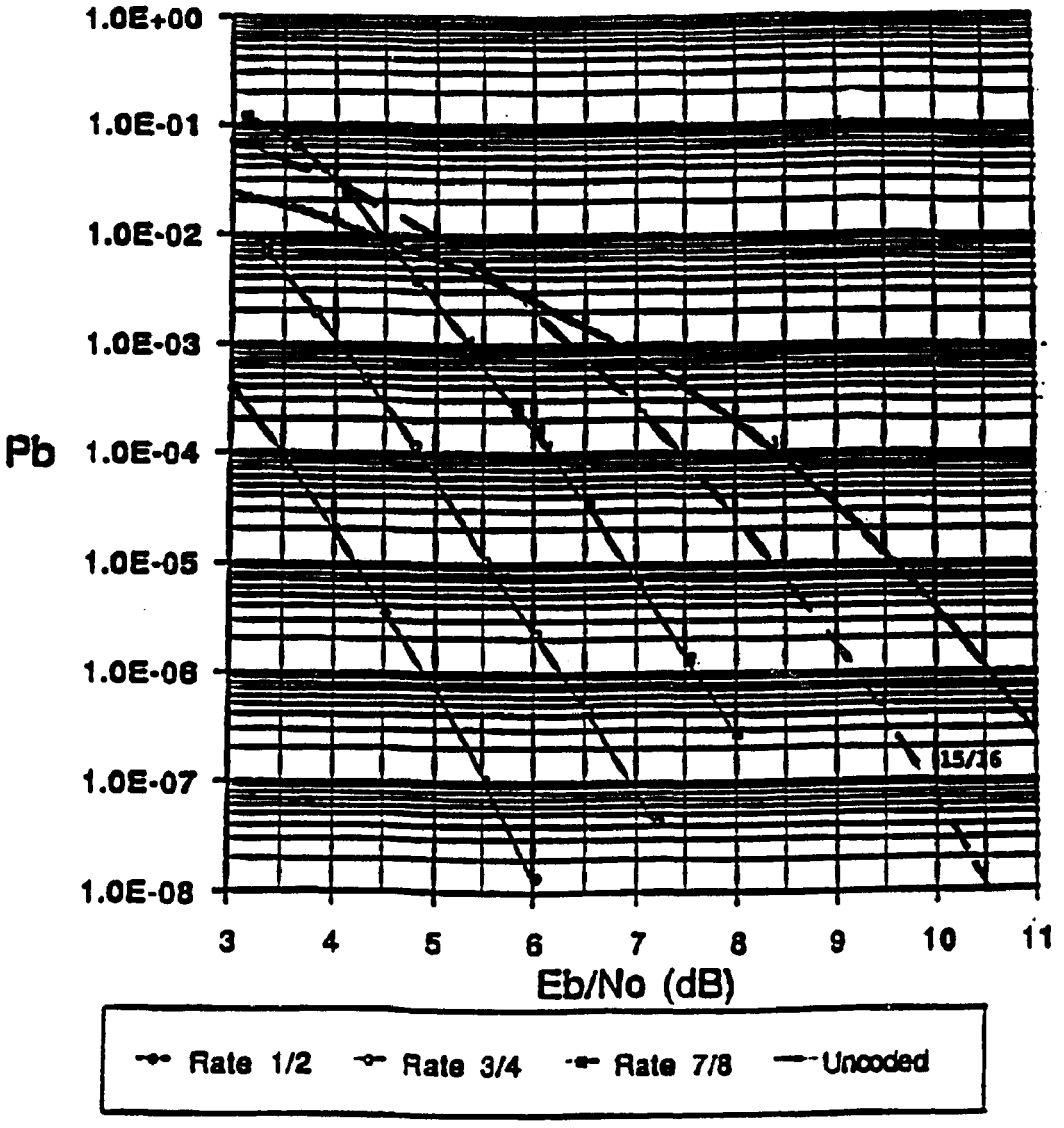

Figure 6.0.8: MPSK distance reduction.

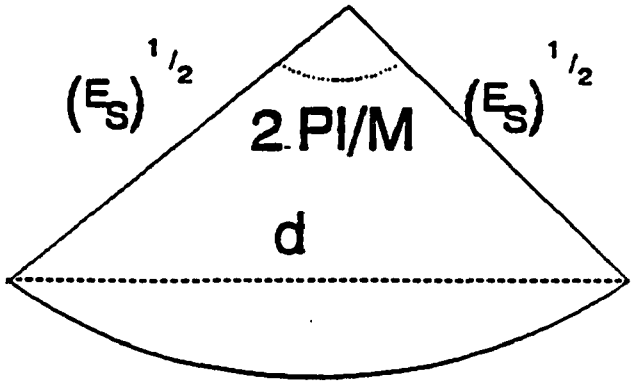

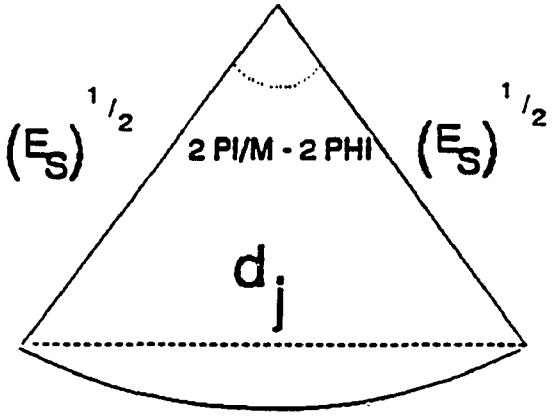

Figure 6.0.9a: phase jitter versus SNR,TC-16PSK, 80 kbps, M=16.

Figure 6.0.9b:timing jitter versus SNR.

Figure 6.0.9c:total loss in dB versus SNR.

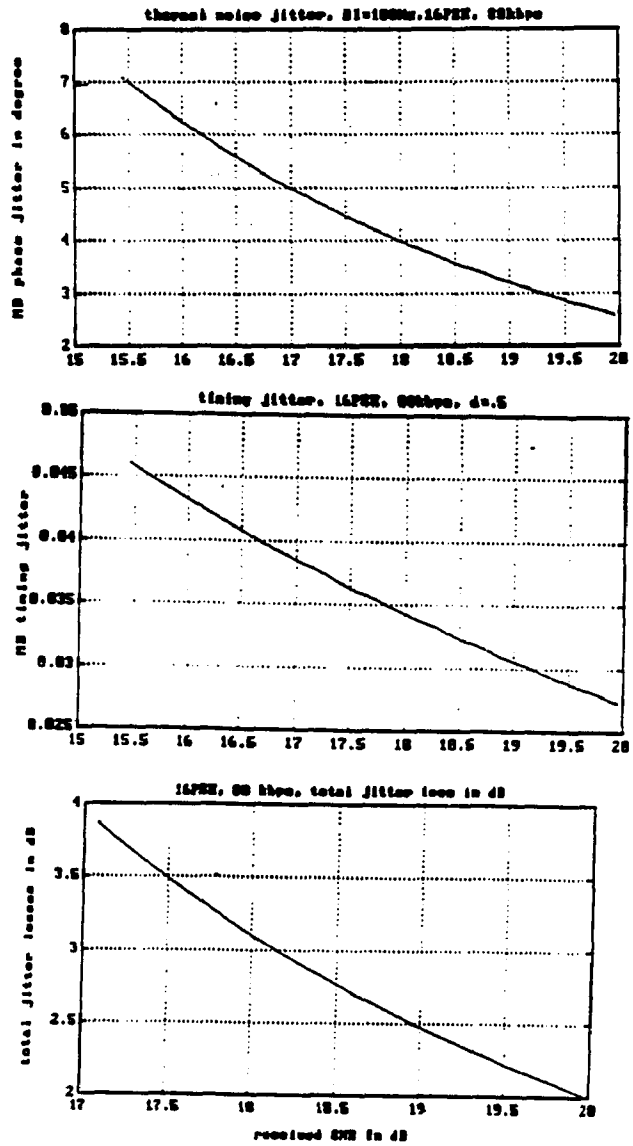

Figure 6.0.10a:phase jitter versus SNR, TC-8PSK, 60 kbps, M=8.

Figure 6.0.10b:timing jitter vs. SNR.

Figure 6.0.10c:total loss vs. SNR.

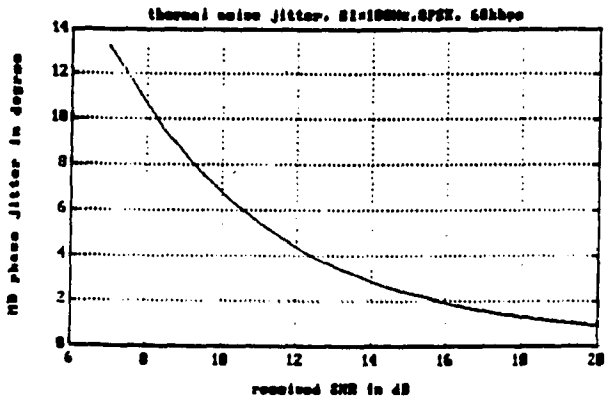

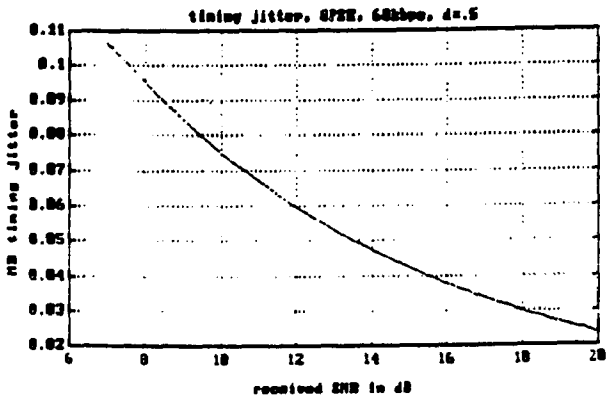

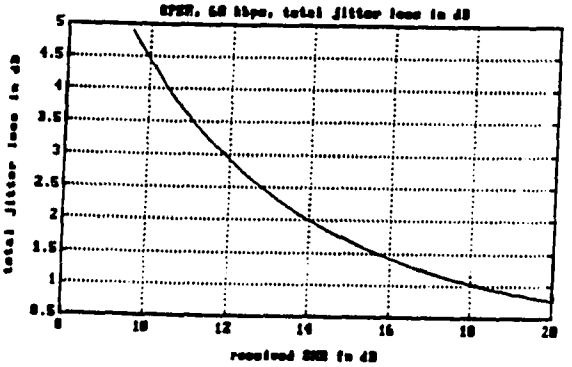

Figure 6.0.11a: phase jitter vs. SNR, TC-QPSK, 40 kbps, M=4.

Figure 6.0.11b: timing jitter vs. SNR.

Figure 6.0.11c: total loss vs. SNR.

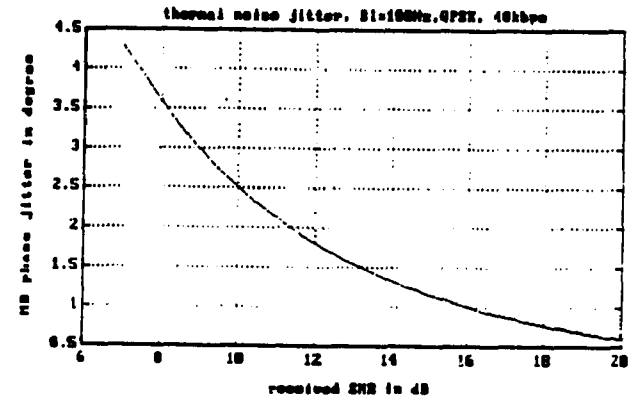

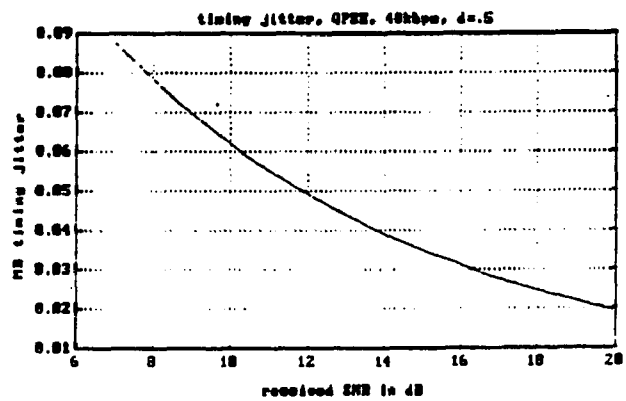

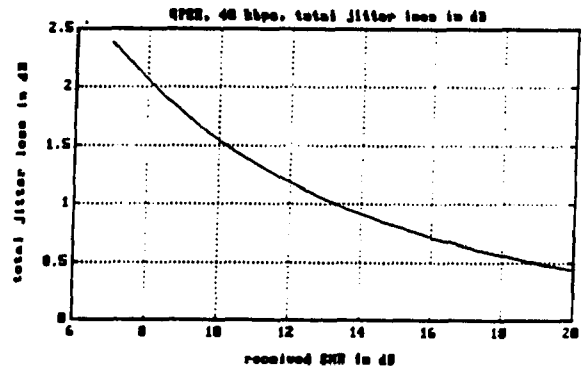

7 RESULTS AND CONCLUSIONS

7.1 SAMPLE SYSTEM

To demonstrate the effects of the doppler spread, the MB phase perturbations, and the jitter losses on the performance of the systems, consider a 1000 km link with the receiver at (x,y,z) the coordinates (500,0,0) and a transmitter at the coordinates (-500,0,0) in the coordinate system of Fig. (2.2.1). The following assumptions, concerning MB system parameters, trail position, orientation, location, velocity, length, decay constant and the wind condition are used in the subsequent analysis:

1) The transmitter power and the antenna gains are chosen such that the initial received SNR can range up to 20 dB.

2) B=40 kHz, W=20 kHz.

3) The carrier frequency is $f = 50$ MHZ, and the carrier wavelength is equal to $\lambda = 6$ m.

4) L=20 km, V=50 km/sec, $(x_t, y_t, z_t) = (400, 20, 100)$,the azimuth angle (relative to XZ plane)=$\gamma = 0°$, the elevation angle (relative to XY plane)=$\eta = 30°$.

5) The decay constant is equal to $\tau = .36$.

6) The wind velocity vector is $\vec{V} = 100\vec{V}_x + 100\vec{V}_y$ m/sec, and the wind gradient is .05 m/sec/m at the tangency point; the wind profile's bandwidth is .25 cycles per km.

7) Maximum allowed bit error rate is $P_{bmax} = 10^{-5}$.

$N_0 = kT_0\left\{\frac{(104)}{(L_R)}(\lambda/15)^{2.3} + F\right\} = 4.89x10^{-20}$ W/Hz,where F=2.5, $L_R = 1.3$, $T_0 = 290$ k°, and $k = 1.38x10^{-23}$ J/k°

', and

9) $f_R = 10$ Hz,$t_R = 15$ msec,$f_W = 30$ Hz,$b/a = 5°$.

A system which operates within the above parameters and constraints is bandwidth-limited

A system which operates within the above parameters and constraints is bandwidth-limited

and power-limited. The wind gradient will cause a doppler rate $\dot{f}_W = 62.5$ Hz/sec. which can last up to $t_W = .266$ seconds. Also the location of the trail, its orientation, and the meteor velocity (equation 3.2.11) lead to $f_D = 4.5$ kHz,$t_D = .2$ seconds.

7.2 BITS-PER-BURST PERFORMANCE RESULTS

Let N be the total number of bits that can be transmitted during one burst. For adaptive trellis-coded MPSK modems, t_B can be expressed as

$$t_B = t_{16} + t_8 + t_4 \tag{7.2.1}$$

$$t_B = \tau\{\varepsilon_1 \ln(\sqrt{\gamma_e/\gamma_{16}}) + \varepsilon_2 \ln(\sqrt{4\gamma_{16}/3\gamma_8}) + \varepsilon_3 \ln(\sqrt{3\gamma_8/2\gamma_4})\} \tag{7.2.2}$$

the total number of bits that can be transmitted over the meteor trail under the assumptions specified in section 7.1 is called N_{MAXIJ}:

$$N_{MAXIJ} = W\tau\{\varepsilon_1\left(\ln\left(\sqrt{\gamma_e/\gamma_{16_J}}\right) + \varepsilon_2 \ln\left(\sqrt{4\gamma_{16_J}/3\gamma_{8_J}}\right) + \varepsilon_3 \ln\left(\sqrt{3\gamma_{8_J}/2\gamma_{4_J}}\right)\right\} - t_{acq_1} f_{b16} + t_{acq_2} f_{b8} - t_{acq_3} f_{b4}$$

(7.2.3)

where

$\tau = .36, \gamma_e = 21.5dB, \varepsilon_1 = 3bps/Hz, \varepsilon_2 = 2bps/Hz, \varepsilon_3 = 1bps/Hz, W = 20kHz, f_{b16} = 60kbps, f_{b8} = 40kbps, f_{b4} = 20kbps.$

t_{acq} can be computed by using equation (5.1.1). This enables us to obtain a maximum-bits-per-burst bound for the adaptive coherent modem described in chapter 6. In these equations, t_M is the time allocated to MPSK, γ_M is MPSK's detection threshold, γ_{MJ} is the extended detection threshold (due to jitter losses), and finally f_{bM} is the MPSK's bit rate.

The total number of bits that can be transmitted over the trail which is not subjected to MB phase perturbations is equal to

$$N_{MAXI} = W\tau\{\varepsilon_1 \ln(\sqrt{(\gamma_e/\gamma_{16})}) + \varepsilon_2 \ln(\sqrt{(4\gamma_{16}/3\gamma_8)}) + \varepsilon_3 \ln(\sqrt{(3\gamma_8/2\gamma_4)})\}$$

(7.2.4)

We can compare the performance of the system under the two operating conditions by dividing (7.2.3) by (7.2.4). The degradation is

$$d_{ADAP.} = \frac{N_{MAXIJ}}{N_{MAXI}} \tag{7.2.5}$$

For the QPSK fixed rate modem introduced in chapter 6, the degradation is equal to

$$d_{FIXED} = \frac{N_{MAX2J}}{N_{MAX2}} = \frac{\left(2W\tau\frac{k}{n}\ln\left(\sqrt{(2\gamma_e/\gamma_{4_j})}\right)\right)}{\left(2W\tau\frac{k}{n}\ln(\sqrt{(2\gamma_e/\gamma_4)})\right)} \tag{7.2.6}$$

where k/n is the code rate.

Table 1 is a survey of coding gains for symmetric and asymmetric trellis codes. Table 2 is a survey of coherent and non-coherent modulation systems. ε is the efficiency factor, while γ_{th} is the SNR needed to keep P_e below 10^{-5}. We can use the following set of values in an example which serves to illustrate the severity of the jitter losses. These values are chosen by consulting tables 1 and 2, and figures 6.09-11.

Example:

Let $(\gamma_{16}, \gamma_8, \gamma_4) = (28.2, 8.2, 2.9) = (14.5, 9.1, 4.6)dB$. and $(\gamma_{16j}, \gamma_{8j}, \gamma_{4j}) = (60.25, 15.9, 5) = (17.8, 12, 7)dB$ be the old and new detection thresholds respectively for the adaptive and fixed rate schemes described in chapter 6. The results are shown in figures (7.2.1-3). The total number of bits that can be transmitted using adaptive coherent modem (16-8-4) and fixed rate modem (QPSK 7/8) are plotted against various initial signal-to-noise ratios (Fig.7.2.1). The principles of operation of the adaptive coherent and fixed rate modems were described in chapter 6 in detail. The complex adaptive coherent modem is outperformed by the QPSK fixed rate modem below 21.5 dB. Figure (7.2.2) demonstrates how two fixed rate modems which use different code rates compare to each other. Code rate 7/8 performs better than 1/2. Furthermore, Figure (7.2.3) illustrates the % reduction in N due to MB

Table 1: Coding gains for symmetric and asymmetric trellis codes.

NUMBER OF MODULATION LEVELS	NUMBER OF STATES IN TRELLIS	GAIN (db) OF SYMMETYRIC MPSK OVER UNCODED M/2 PSK	GAIN (db) OF ASYMMETRIC MPSK OVER SYM. CODED MPSK
4	2	1.76	1.25
4	4	3.98	.28
4	8	4.77	.46
8	2	1.116	1.9
8	4	3.01	0.0
8	8	3.60	0.0
8	16	4.13	.024
16	2	1.00	2.01
16	4	3.54	.18
16	8	4.014	.32
16	16	4.440	0.00

Table 2: Spectral efficiency factor.

	M	ϵ SPEC. EFF.	SNR γ_{th} (db)	FORMULA FOR SPECTRAL EFFICINCY
MPSK COHERENT SIGNALING	2 4 8 16	1 2 3 4	9.6 9.6 12.9 17.5	$\epsilon = \log_2(M)$
MFSK ORTHOGONAL COHERENT	2 8 16 32	1 .75 .5 .3125	12.6 8.4 7.4 6.6	$\epsilon = 2\log_2(M)/M$
MFSK BIORTHOGONAL COHERENT	2 8 16 32	2 1.5 1 .625	9.6 8.3 7.4 6.5	$\epsilon = 4\log_2(M)/M$
MFSK NON-COHERENT SIGNALING	2 8 16 32	.5 .375 .25 .15625	13.4 9.4 8.2 7.2	$\epsilon = \log_2 M/M$

Figure 7.2.1: Adaptive vs. fixed modem.

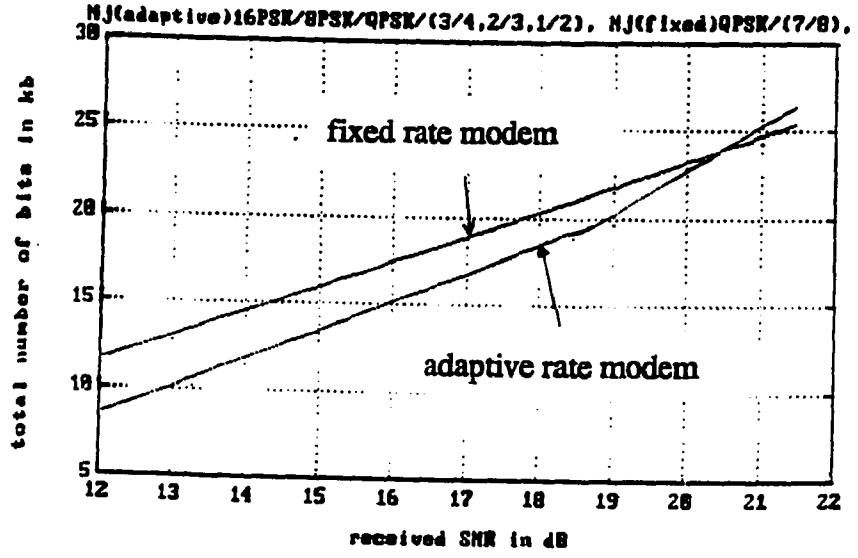

Figure 7.2.2: Two fixed rate modems.

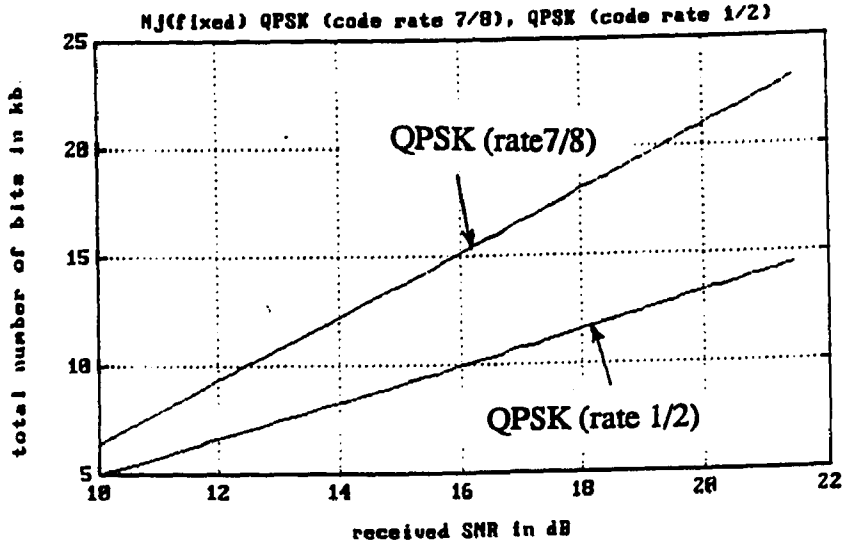

Figure 7.2.3: % reduction in N due to jitter losses.

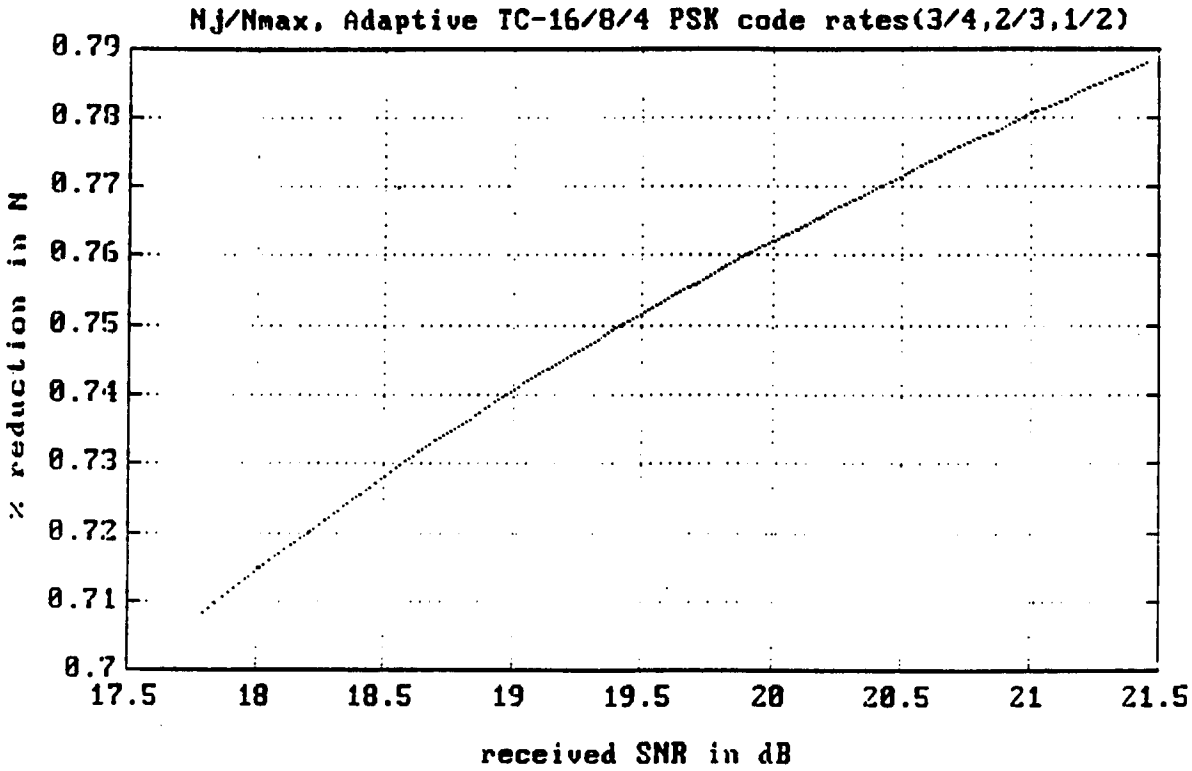

7.3 THROUGHPUT

The throughput is defined as the average continuous transmission rate in bits per second. An appropriate modulation-dependent formula for the throughput is shown to be (Equation A.7)

$$T = k_1 \sqrt{\frac{\varepsilon}{\gamma_{old}}} \tau \ln\left(\sqrt{\frac{\gamma_e}{\gamma_{old}}}\right) \qquad (A.7)$$

This equation can serve as a basis for comparing the performance of various modulation schemes. A simple performance measure that proves useful in determining the MB system degradation due to phase perturbations is the relative throughput reduction which is defined as

$$r_{FIXED} = \frac{T_{new}}{T} = \sqrt{\frac{\gamma_{old}}{\gamma_{new}}} \frac{(\ln(\sqrt{\gamma_e/\gamma_{new}}))}{(\ln(\sqrt{\gamma_e/\gamma_{old}}))} \qquad (7.3.1)$$

where $\gamma_{new} = \gamma_{old} + \Delta$ (equation 6.0.9) and T_{new} is the new threshold due to the jitter losses and the corresponding throughput respectively. The expression provides a good physical insight into the loss mechanism. The inter-arrival time is decreased due to the increase in the detection threshold. This fact is reflected in the term $\sqrt{\left(\frac{\gamma_{old}}{\gamma_{new}}\right)}$. The term $\frac{(\ln(\sqrt{(\gamma_e/\gamma_{new})}))}{(\ln(\sqrt{(\gamma_e/\gamma_{old})}))}$ corresponds to the reduction in burst duration due to threshold extension.

The reduction in throughput for an adaptive rate system(r_{ADAP}) is derived by noting that the meteor trails can be divided into three categories. One type of trail has electron line density such that the modem can start its transmission by employing TC-16PSK. The probability of occurrence of such an event is equal to

$$p_{16} = P\{\gamma_{16} < \gamma_e < \gamma_u\} = P\{q_{16} < q_e < q_u\} = \int_{(q_{16})}^{(q_u)} f_q(q)dq$$

where [8]

$$f_q(q) = .6q_{\min}^{.6}\frac{q_u^{.6}}{(q_u^{.6} - q_{\min}^{.6})}q^{-.6}$$

is the probability density function of the electron line density. q_M is the minimum line density required to start the transmission utilizing MPSK. For this category of trails the throughput reduction is

$$r_{ADAP16} = \sqrt{(\gamma_{16}/\gamma_{16J})}\, d_{ADAP}$$

Similarly, the probabilities of occurrence of the other two trail types are

$$p_8 = P\{\gamma_8 < \gamma_e < \gamma_{16}\}$$

and

$$p_4 = P\{\gamma_4 < \gamma_e < \gamma_8\}$$

with

$$r_{ADAP8} = \sqrt{(\gamma_8/\gamma_{8J})}\, d_{ADAP}, \gamma_e \in (\gamma_8, \gamma_{16})$$

and

$$r_{ADAP4} = \sqrt{(\gamma_4/\gamma_{4J})}\, d_{ADAP}, \gamma_e \in (\gamma_4, \gamma_8)$$

Combining these equations, r_{ADAP} becomes

$$r_{ADAP} = p_4 r_{ADAP4} + p_8 r_{ADAP8} + p_{16} r_{ADAP16} \tag{7.3.2}$$

where r_{ADAP} is the overall reduction in the adaptive coherent scheme. An example using typical numbers can demonstrate the severity of the degradation for a adaptive rate system (r_{ADAP}). The example is worked out for the following numbers

$C_u = 9.78x10^{-42}, \gamma_u = 100, \gamma_{16} = 30, \gamma_{16J} = 60, \gamma_8 = 12, \gamma_{8J} = 24, \gamma_4 = 5, \gamma_{4J} = 10$.The probabilities will be equal to $(p_{16}, p_8, p_4) = (.41, .23, .36)$ and $(d_{ADAP}, d_{ADAP8}, d_{ADAP4}) = (.481, .585, .3535)$. r_{ADAP} equals .46. As seen by using equation 7.3.1 the throughput of a QPSK fixed rate system is

reduced by a factor of $r_{FIXED} = .55$.

8 FUTURE WORK

This dissertation has been primarily directed towards solving the theoretical pre-requisites for optimum channel coding of MB communication systems. The new channel model developed in this work opens up new research possibilities. The findings developed in this dissertation regarding the inefficiency of adaptive coherent MB modems (Fig. 7.2.1 and 7.2.3), justifies and points toward implementing high data rate MB modems employing non-coherent detection.

Interestingly, Hirono et Al [18] have developed a new non-coherent Narrow-band FSK system which achieves 2 bits/sec/Hz at 14 dB ($P_e = 10^{-3}$). Further research in this area could lead to the design of digital FM systems with b>2 bits/sec/Hz. This system have three advantages which make it ideal for building high data rate meteor burst modems. First, there is no need to lock into phase and frequency (non-coherent detection). Second, the adaptive equalizer incorporated in the receiver compensates for the head-echo induced phase jitter. And finally, they are spectrally efficient unlike conventional Narrowband FSK systems.

9 APPENDIX A

THROUGHPUT

In this appendix an equation is derived for the throughput, the importance of the throughput equation lies in the fact that the modulation-dependent terms are identified and isolated in the equation. Throughput is defined as the average continuous transmission rate in bits per seconds.

The duty cycle is defined as the burst duration over channel inter-arrival time

$$D = \frac{t_B}{t_I} \tag{A.1}$$

where t_B is the burst duration and is equal to

$$t_B = \tau \ln\left(\frac{q_i}{q_{\min}}\right) \tag{A.2}$$

where q_i is the initial electron line density. $q_{\min}$ is defined as the minimum electron line density required to support a specific transmission and it is equal to

$$q_{\min} = \sqrt{\frac{N_0}{C_u} R\, erfc^{-1}(P_{bmax})} \tag{A.3}$$

where

$$erfc^{-1}(P_{bmax}) = \left(\frac{E_b}{N_0}\right)_{req} = \gamma_{old} \tag{A.4}$$

The meteor arrival rate which is the inverse of the inter-arrival time is equal to

$$\frac{1}{t_I} = \frac{k}{q_{\min}} \tag{A.5}$$

where k is a constant. Substituting A.2 and A.5 into A.1 yields

$$D = \frac{t_B}{t_I} = \frac{k}{q_{\min}} \tau \ln\left(\frac{q_i}{q_{\min}}\right)$$

$$D = k\tau\sqrt{\frac{C_u}{(N_0 R\gamma_{old})}}\ln\left(\sqrt{\frac{\gamma_e}{\gamma_{old}}}\right) \qquad (A.6)$$

Throughput, defined as the average continuous transmission rate in bits per seconds, is equal to

$$T = RD = k_1\sqrt{\frac{\varepsilon}{\gamma_{old}}}\tau\ln\left(\sqrt{\frac{\gamma_e}{\gamma_{old}}}\right) \qquad (A.7)$$

where γ_{old} is the detection threshold (the jitter losses are not considered here). The spectral efficiency factor ($\varepsilon = \frac{R}{W}$) and γ_{old} are the modulation-dependent terms. $\gamma_e = q_i^2\frac{C_u}{(N_0 R)}$ = is the initial signal-to-noise ratio.

10 REFERENCES

[1] G.W. Pickard, " A note on the reception of meteor showers and radio reception " Proc. IRE, vol 19, pp 1160-1170; July 1931

[2] J.S. Hey and G.S.Stewart, "derivation of meteor stream radiants by radio reflexion methods" Nature, vol. 158, pp 481-482; Oct. 1946

[3] N. Herlofson, 1948, Rep. Progr. Phys.,11, 444(London:Physical Society)

[4] D.W.R. Mckinley, " Meteor Science and Engineering," McGraw-Hill Book Company, Inc.,New York, N.Y. ;1961

[5] G.R. Sugar, " Radio propagation by reflection from meteor trails" Proc. Of IEEE. pp. 116-136, Feb. 1964

[6] L.A. Manning, "Air motions and the fading diversity, and aspect sensitivity of meteoric echos," J. Geophys. Res., vol. 64, pp 1415-1425; Oct. 1959

[7] J.A. Weitzen etal, "High-resolution multipath measurements of the meteor scatter channel," Radio Science, vol. 19, pp. 375-381 Jan-Feb. 1984

[8] E. Hibshoosh, " A study of a Meteor Burst Communication System," Ph.D. Dissertation, C.C.N.Y., New York, June 1987

[9] J.S. Greenhow, E.L.Neufeld,"Measurement of turbulence in the upper atmosphere," Proc. Of the Physical Society, vol 74 July 1959

[10] J.S.Greenhow, E.L. Neufeld,"Phase changes and Resonance effects in radio echos from meteor trails," Proc. Of Physical Society, Jan. 1957

[11] T.R. Kaiser 1955 Atmos. Terr. Phys., Meteors :special suppl. 2,73.

[12] W.C. Lindsey, M. Chie, Phase Locked Loops, pp 1-27 IEEE Press, New York 1986

[13] F.M. Gardner, Phaselock Techniques, 2nd. ed. New York: Wiley, 1968

[14] H.Meyr, L.Popken, "Phase acquisition statistics of phase locked loops," IEEE Trans. on Comm. VOL. COM-28, No. 8, Aug. 1980

[15] A.J. Viterbi, Principles of coherent communication, New York: McGraw Hill, 1966

[16] W.C. Lindsey and M.K. Simon, "Carrier synchronization and detection of polyphase signals," IEEE Trans. Comm. part I, pp. 441-454, June1972

[17] H. Taub and D.L. Schilling,Principles of communication systems, 2nd. ed,McGraw-Hill Book Company, New York 1986

[18] M. Hirono, etal, "Multi -level decision method for band-limited digital FM with limiter-

discriminator detection," IEEE J. Select. Areas Comm.,vol SAC-2, pp. 498-506, July 1984

[19] B. Sklar, Digital Communications: Fundementals and Applications, Prentice Hall, Englewood Cliffs,1988

[20] D. Divsalar, M. Simon, J. Yen.,"Trellis Coding with asymmetric modulations," IEEE Trans. on Comm. vol. COM-35, pp. 130-141, Feb. 1987

[21] S.S. Chang "A Feedback Adaptive Variable Rate Meteor Burst Communication Systems", IEEE int. conference on communications,1988, conference Records, volume 1, pp. 0423- 0429

[22] D.L. Schilling, R. Bozovic," On the Performance Of Spectrally Efficient Trellis Coded FM Modulation employing Non-Coherent FM demodulation," IEEE JSA in comm. vol. 7 No. 9, pp. 1318-1327, Dec. 1989

[23] Manning, L.A. And Eshleman, V.R., "Meteors in the ionosphere", Proc. IRE. 47, no. 2, pp 186-99, Feb. 1959.

[24] Weitzen, J.A. "A Study of the Ground Illumination Footprint of Meteor Scatter Communication", IEEE Trans. on Comm. vol. 38 no. 4, pp. 426-430, April 1990.

[25] Bartholome, P.J. And Vogt, I.M.,"COMET- A new meteor burst system incorporating ARQ and diversity reception", IEEE trans. on comm., COM-16, no. 2, pp. 268-278, April 1968.

[26] Hannum, A.J.,et Al, "Air-to-ground meteor scatter communications system", IRE Trans. Com. Syst.,CS-8,no. 2, pp. 113-33, 1960.

[27] Lindemann, F.A., And Dobson, G. M. B.,1923, Proc. Roy. Soc., A102, 411-437, "A theory of meteors,and the density and temperature of the outer atmosphere to which it leads."

[28] Opik, E.,"Physics of the meteor flight in the atmosphere." Interscience Publishers,Inc.,New York,1958.

[29] Whipple, F.L.,"Meteors and the earth's upper atmosphere", Rev. Mod. Phys.,15,246-264, 1943.

[30] D.W. Brown, " A physical meteor burst propagation model and some significant results for communication system design," IEEE JSAC,vol. SAC-3, pp. 745-755, may 1986.

[31] J.A. Weitzen, "Predicting the arrival of meteors useful for meteor burst communication," Radio Sci., vol. 21, no. 6, pp. 1006-1020, Nov.-Dec. 1986.

[32] P.S. Cannon, "Polarization rotation in meteor burst communication systems," Radio Sci., vol. 21,no. 3, pp.501-511, May 1986.

[33] L.A. Maynard, "Meteor burst communication in the arctic," in Ionospheric Radio Communications: Proc. NATO Institute on Ionospheric Radio Communications in the Arctic, Finse, Norway, Apr. 13-19,1967. New York: Plenum, 1968, pp. 165-173.

[34] J.A. Weitzen,etal," Characterizing the multipath and Doppler profiles of the high latitude meteor burst communication channel," IEEE Trans. Comm. pp. 1050-1058, 1987.

[35] J.A.Weitzen,etal, " An estimate of the capacity of the meteor burst channel," IEEE Trans. Comm.,vol. COM-32, no. 8, pp. 972-974, Aug. 1984.

[36] J.A.Weitzen, "Communicating via meteor burst at short ranges," IEEE Trans. Commm.,vol. COM-35, Nov. 1987.

[37] G. M. Djuknic,' An analysis of ARQ and hybrid FEC-ARQ transmission over a meteor burst channel," Ph.D. Dissertation, C.C.N.Y., N.Y. June 1988.

[38] J.M.Jacobsmeyer, "Digital signal design for meteor-scatter communications," MS Thesis, Cornell University, Aug 1987.

[39] D.L. Schilling, " High Data Rate Meteor Burst Communications," ICC 89

[40] M.W.Abel, "Meteor burst communications: bits per burst performance bounds," IEEE Trans. Comm. vol.34,no.9, pp. 927-936, Sep. 1986.

[41] M.Pursley, S.D.Sandberg " Variable-rate coding for meteor burst communications," IEEE Trans. Comm. vol. 37,no. 11, pp. 1105-1112, Nov. 1989.

[42] J.M. Jacobsmeyer," Adaptive Trellis Coded Modulation for bandlimited meteor burst

channel," ICC 88

[43] C.O.Hines and P.A. Forsythe, " The forward scattering of radio waves from overdense trails," Can. J. Phys., vol. 35,pp. 1033-1041, Sept. 1957.

[44] R.J. Carpenter and G.R.Ochs, "High resolution, pulse measurements of meteor burst propagation at 41 Mc/s over a 1295km path," J.Res. Nat. Bur. Standards, vol.64D, no. 3,pp.249-262, May-June 1962.

[45]G.R.Sugar et al,"Elementary considerations of effects of multipath on meteor burst communications," J. Res. Nat. Bur. Standards, vol. 64D,no.5, pp. 495-500, Sep. 1960.

[46] Manual of Regulations and Procedures for Federal Radio Frequency Management,Annex J, Guidance for Determination of Necessary Bandwidth, National Telecommunications and Information Administration.

[47] L.B. Milstein, D.L. Schilling, R.L.Pickholtz, J. Sellman, S. Davidovici, A. Pavelcheck, A. Schneider, and G. Eichmann, "Performance of meteor burst communication channels," IEEE J. Select. Areas Commun., vol. SAC-5,pp. 146-154, Feb. 1987.

[48] D.L. Schilling, G.R. Lomp, L.A. Lundberg," High Data Rate Meteor Burst Communications," ICC 90, Az.

[49] J.S. Greenhow, "Characteristics of radio echoes from meteor trails: III The behavior of the

electron trails after formation," Proc. Phys. Soc., London, B, 65, 169-181, 1952.

[50] F.L. Whipple," Winds in the upper atmosphere by meteor trail photography," J. Meteor, 10, 390-392, 1953.

[51] J. S. Greenhow, "Systematic wind measurements at altitudes of 80-100 km using radio echoes from meteor trails, Phil. Mag., 45, 471-490, 1954.

[52] N. H. Rudie, " The relative distribution of observable meteor trails in forward scatter meteor communications,"Ph.D. Dissertation, Montana State Univ., Bozeman, 1967.

[53] C.D. Ellyett, and J. G. Davies, "Velocity of meteors measured by diffraction of radio waves from trails during formation." Nature, 161, 596-597, 1948.

[54] L.A. Manning, "The theory of radio detection of meteors," J. App. Phys., 19, 689-699, 1948.

[55] Chamanlal and K. Venkatamaran, "Whistling meteors- a doppler effect produced by meteors entering the ionosphere," Electrotechnics 14, 28-40, 1941.

[56] W.R. Vincent, et al,"Analysis of oblique meteor propagation data from the communication viewpoint," Proc. Of the IRE, pp. 1701-1707,1957.